Final version available at Wiley : http://dx.doi.org/10.1002/nag.2425

Adaptive isogeometric finite element analysis of steady-state groundwater flow

Y. W. Bekele[1]*, T. Kvamsdal[2], A. M. Kvarving[3], S. Nordal[1]

[1]*Department of Civil and Transport Engineering, Norwegian University of Science and Technology, Trondheim, Norway*

[2]*Department of Mathematical Sciences, Norwegian University of Science and Technology, Trondheim, Norway*
[3]*Department of Applied Mathematics, SINTEF ICT, Trondheim, Norway*

SUMMARY

Numerical challenges occur in the simulation of groundwater flow problems due to complex boundary conditions, varying material properties, presence of sources or sinks in the flow domain or a combination of these. In this paper, we apply adaptive isogeometric finite element analysis using locally refined (LR) B-splines to address these types of problems. The fundamentals behind isogeometric analysis and LR B-splines are briefly presented. Galerkin's method is applied to the standard weak formulation of the governing equation to derive the linear system of equations. A posteriori error estimates are calculated to identify which B-splines should be locally refined. The error estimates are calculated based on recovery of the L_2-projected solution. The adaptive analysis method is first illustrated by performing simulation of benchmark problems with analytical solutions. Numerical applications to two-dimensional groundwater flow problems are then presented. The problems studied are flow around an impervious corner, flow around a cutoff wall and flow in a heterogeneous medium. The convergence rates obtained with adaptive analysis using local refinement were, in general, observed to be of optimal order in contrast to simulations with uniform refinement.

Received . . .

KEY WORDS: adaptive refinement; isogeometric analysis; a posteriori error estimates; groundwater flow

1. INTRODUCTION

Finite element modeling of groundwater flow problems has been a subject extensively studied by several researchers over the past decades. The earliest studies which addressed this problem include the finite element analysis of seepage through dams by Finn [1], Galerkin's method in aquifer analysis by Pinder and Frind [2], finite element modeling of flow in saturated-unsaturated porous media by Reeves and Duguid [3] and a three-dimensional finite element model for a multiaquifer system by Gupta *et al.* [4]. Some studies proposed improvements to the finite element modeling of groundwater flow based on the numerical challenges observed in previous studies. Yeh [5] proposed an approach to eliminate problems of discontinuity in the Darcy velocity field, which result when the
taking the derivatives of the finite element computed pressure field. Botha and Bakkes [6] studied the convergence of the Galerkin finite element method when applied to groundwater flow problems,
with special reference to quadrature effects and the accuracy of the solution. Tharp [7] presented an enriched finite element simulation of groundwater flow by introducing a new quadrilateral element

*Correspondence to: Yared Worku Bekele, Department of Civil and Transport Engineering, NO-7491, Trondheim, Norway. E-mail: yared.bekele@ntnu.no

to enable accurate modeling with coarse meshes. Dogrul and Kadir [8] presented a finite element post-processing technique to compute mass conserving flow rates at element faces.

The numerical challenges that occur in the simulation of groundwater flow problems may be induced by the complexity of the boundary conditions in the flow domain, the varying hydraulic conductivity properties of the porous material, the presence of sources or sinks, such as an infiltration well, or a combination of these. One of the approaches used to treat such numerical difficulties is to superpose an analytical solution in the vicinity of the problem area with a numerical model in the rest of the domain. Analytical solutions are, however, difficult to obtain for most physical problems involving groundwater flow. The other approach is to use special numerical techniques to address the singularity or discontinuity problems. We briefly look at some of the techniques proposed by some researchers for different types of problems.

Some of the singularities that arise in the numerical simulation of groundwater flow were studied and discussed by Lafe *et al.* [9]. The singularities considered are flow around a sharp corner where the velocity goes to infinity, flow between zones of different hydraulic conductivity, flow around a cutoff wall and the presence of sources or sinks in the flow domain. The effects of the different singularities were studied and discussed. Weak singularities as in the case of flow between zones of varying hydraulic conductivity were treated by concentrating integration points at the area of the singularity. The use of special elements is recommended for stronger singularities such as flow around a cutoff wall.

Groundwater flow with a free seepage surface is one of the problems that requires a special treatment due to the complex boundary conditions. The derivative of the hydraulic potential goes to infinity at the point of intersection between the free surface and the downstream face of the dam. Even though we are not dealing with a free surface problem in the present work, we review the numerical techniques proposed by various researchers as it is a related problem to our scope. Liang and Zhang [10] presented a mathematical study of the finite element method for a unidimensional single-phase nonlinear free boundary problem in groundwater flow. Neuman and Witherspoon [11] proposed an iterative approach to steady seepage of groundwater with a free surface. Larabi and De Smedt [12] studied the numerical solution of groundwater flow involving free boundaries by a fixed finite element method by iteratively adjusting the moving boundaries. An adaptive finite element approach for the free surface seepage problem was presented by Rank and Werner [13]. They used a posteriori error estimates and adaptive mesh refinement such that the influence of singularities on the convergence rate disappears. Sharif and Wiberg [14] used an interface capturing technique to solve seepage flow problems with free surface in porous media and studied two and three-dimensional seepage through dams. The performance of a finite element adaptive mesh algorithm for seepage flow with a free surface was analyzed by Borieu and Bruch [15]. The algorithm was especially tested in order to enable parallel computations. A slightly different approach to the free surface problem was presented by Jie *et al.* [16] where they apply the natural element method (NEM) by constructing shape functions based on Voroni diagrams. They argue that the method is more suitable for the analysis of seepage problems with a free surface than the finite element method. Adaptive error analysis for seepage problems was presented by Burkley and Bruch [17] based on the Zienkiewicz-Zhu error estimator.

The other source of numerical challenges in the computation of groundwater flow problems is the complexity of the material properties in the flow domain. Flow between zones of different hydraulic conductivity represents a less severe discontinuity which may be treated by a finer mesh at the intersection of the different zones. Heterogeneous aquifers on the other hand represent a more complex case. Smaoui *et al.* [18] studied the modeling of groundwater flow in heterogeneous porous media by the finite element method. Cao and Kitanidis [19] presented a methodology for the computation of flow in a heterogeneous isotropic formation using adaptive mesh refinement. Dual equations with hydraulic head and stream function were solved numerically. They claim that the application of a standard finite element method requires a large number of nodes to model flow in high-contrast formations. However, the number of unknowns to achieve a certain accuracy may be reduced by adaptive mesh refinement procedures that rely on a posteriori error estimates to identify areas where refinements are most needed.

The presence of sources or sinks in the flow domain creates areas of large changes in the hydraulic gradient. Such a problem for unconfined aquifers with an infiltration well was studied using adaptive mesh refinement by George and Thomas [20]. They performed simulation on flow domains with isotropic as well as heterogeneous hydraulic conductivity fields. The simulations were performed starting with a coarse mesh and refinement/coarsening steps were applied depending on the computed errors.

In this paper, we address some of the numerical challenges observed in computational models for groundwater flow problems using adaptive isogeometric finite element analysis. We use LR B-splines, first proposed by Dokken *et al.* [21], and later applied to adaptive isogeometric analysis by Johannessen *et al.* [22]. First, the governing equations of steady-state groundwater flow are presented. The fundamentals of isogeometric analysis are then briefly discussed by introducing B-splines and Non-Uniform Rational B-splines (NURBS). LR B-splines, which allow local refinement unlike B-splines and NURBS, are then presented. In the numerical examples section, the method is first applied to benchmark problems with analytical solutions and then to flow problems around an impervious corner, around a cutoff wall and in a heterogeneous formation.

2. GOVERNING EQUATIONS

The governing equation for groundwater flow can be obtained by deriving the fluid mass conservation equation for a given porous medium. The general form of the governing equation for groundwater flow is given by:

$$S\frac{\partial h}{\partial t} = \frac{\partial}{\partial x}\left(k_x(h)\frac{\partial h}{\partial x}\right) + \frac{\partial}{\partial y}\left(k_y(h)\frac{\partial h}{\partial y}\right) + \frac{\partial}{\partial z}\left(k_z(h)\frac{\partial h}{\partial z}\right) + f \tag{1}$$

where S is the so called specific storativity, h is the unknown hydraulic head, k_x, k_y, k_z are the components of the hydraulic conductivity matrix along the principal axes and f represents a source/sink term for the flow. The above equation generally represents transient groundwater flow, i.e. the hydraulic head varies with time, and the flow may be saturated or unsaturated. Unsaturated flow is characterized by a condition where the hydraulic conductivity is a function of the unknown hydraulic head. In this paper, we are interested in saturated flow under steady-state conditions. For such a case, the governing equation reduces to:

$$\frac{\partial}{\partial x}\left(k_x\frac{\partial h}{\partial x}\right) + \frac{\partial}{\partial y}\left(k_y\frac{\partial h}{\partial y}\right) + \frac{\partial}{\partial z}\left(k_z\frac{\partial h}{\partial z}\right) + f = 0 \tag{2}$$

which may be written in a more compact form as:

$$\nabla \cdot (\mathbf{k}\nabla h) + f = 0 \tag{3}$$

where $\mathbf{k}$ is the hydraulic conductivity matrix for general three-dimensional condition given by:

$$\mathbf{k} = \begin{bmatrix} k_x & 0 & 0 \\ 0 & k_y & 0 \\ 0 & 0 & k_z \end{bmatrix} \tag{4}$$

The hydraulic head represents the total energy driving the flow and is expressed per unit weight at any point in the flow domain as:

$$h = \frac{p^w}{\gamma^w} + z + \frac{v^2}{2g} \tag{5}$$

where p^w/γ^w is the pressure head, γ^w is the unit weight of water, z is the elevation head and $v^2/2g$ is the velocity head, with g being the acceleration due to gravity. The velocity head is usually neglected since steady-state groundwater flow velocities are usually very small. It can be shown that the first

term in Eq. 3 represents the divergence of Darcy's velocity, which is given by:

$$\mathbf{v} = -\frac{1}{\gamma^w}\mathbf{k}\left(\nabla p^w - \rho^w \mathbf{g}\right) \tag{6}$$

for a flow driven by pressure gradients and gravity $\mathbf{g} = -g\nabla z$. We can now introduce the proper boundary conditions and write the strong form of the problem as:

$$\begin{aligned} \nabla \cdot \mathbf{v} &= f \quad \text{in } \Omega \\ p^w &= \hat{p}^w \quad \text{on } \Gamma_D \\ \mathbf{v} \cdot \mathbf{n} &= q^w \quad \text{on } \Gamma_N \end{aligned} \tag{7}$$

where Ω represents the groundwater flow domain, $\hat{p}^w$ is the imposed pressure on the Dirichlet boundary Γ_D, q^w is the water flux on the Neumann boundary Γ_N and $\mathbf{n}$ is the normal to the boundary. Here, we have the overall boundary to Ω as $\Gamma = \Gamma_N \cup \Gamma_D$. The pressure $p^w : \Omega \to \mathbb{R}$ is our primary unknown and the Darcy velocity $\mathbf{v} : \Omega \to \mathbb{R}$ can be determined as a secondary solution.

3. ISOGEOMETRIC ANALYSIS

3.1. Fundamentals

Since its first introduction by Hughes *et al.* [23], isogeometric analysis (IGA) has been successfully applied to several areas of engineering mechanics problems. The fundamental aim for the introduction of IGA was the idea of bridging the gap between computer-aided design (CAD) and finite element analysis (FEA). The main concept behind the method is the application of the same basis functions used in CAD for performing finite element analysis. In the process of its application to various engineering problems, IGA has shown advantages over the conventional finite element method, for instance the ease of performing simulations using elements with higher order continuity.

The current standard basis functions in CAD are B-splines and NURBS (Non-Uniform Rational B-splines). To overcome the limitations of B-splines and NURBS, such as water tightness in CAD and local refinement in analysis, other spline technologies have been proposed. These include T-Splines introduced by Sederberg *et al.* [24] and LR B-splines by Dokken *et al.* [21]. In this paper, LR B-splines are used for the simulation of steady-state seepage problems. Prior to that, the fundamental concepts behind IGA are briefly presented here for reference.

3.1.1. B-splines and NURBS. We start the discussion on B-splines and NURBS by first defining a *knot vector*. A knot vector in one dimension is a non-decreasing set of coordinates in the parameter space, written as $\Xi = \{\xi_1, \xi_2, ..., \xi_{n+p+1}\}$, where $\xi_i \in \mathbb{R}$ is the i^{th} knot, i is the knot index, $i = 1, 2, ..., n + p + 1$, p is the polynomial order, and n is the number of basis functions. Knot vectors may be uniform or non-uniform depending on whether the knots are equally spaced in the parameter space or not.

A univariate B-spline curve is parameterized by a linear combination of n B-spline basis functions, $\{N_{i,p}\}_{i=1}^{n}$. The coefficients corresponding to these functions, $\{\mathbf{B}_i\}_{i=1}^{n}$, are referred to as control points. The B-spline basis functions are recursively defined starting with piecewise constants ($p = 0$):

$$N_{i,0}(\xi) = \begin{cases} 1 & \text{if } \xi_i \leq \xi < \xi_{i+1} \\ 0 & \text{otherwise} \end{cases} \tag{8}$$

For higher-order polynomial degrees ($p \geq 1$), the basis functions are defined by the Cox-de Boor recursion formula:

$$N_{i,p}(\xi) = \frac{\xi - \xi_i}{\xi_{i+p} - \xi_i} N_{i,p-1}(\xi) + \frac{\xi_{i+p+1} - \xi}{\xi_{i+p+1} - \xi_{i+1}} N_{i+1,p-1}(\xi) \tag{9}$$

B-spline geometries, curves, surfaces and solids, are constructed from a linear combination of B-spline basis functions. Given n basis functions $N_{i,p}$ and corresponding control points $\mathbf{B}_i \in \mathbb{R}^d, i =$

$1, 2, ..., n$, a piecewise polynomial B-spline curve is given by:

$$\mathbf{C}(\xi) = \sum_{i=1}^{n} N_{i,p}(\xi)\mathbf{B}_i \tag{10}$$

Similarly, for a given control net $\mathbf{B}_{i,j}, i = 1, 2, ..., n, j = 1, 2, ..., m$, polynomial orders p and q, and knot vectors $\Xi = \{\xi_1, \xi_2, ..., \xi_{n+p+1}\}$ and $\mathcal{H} = \{\eta_1, \eta_2, ..., \eta_{m+q+1}\}$, a tensor product B-spline surface is defined by:

$$\mathbf{S}(\xi, \eta) = \sum_{i=1}^{n}\sum_{j=1}^{m} N_{i,p}(\xi)M_{j,q}(\eta)\mathbf{B}_{i,j} \tag{11}$$

B-spline solids are constructed in a similar way as B-spline surfaces from tensor products over a control lattice.

NURBS are built from B-splines to represent a wide array of objects that cannot be exactly represented by polynomials. A NURBS entity in $\mathbb{R}^d$ is obtained by projective transformation of a B-spline entity in $\mathbb{R}^{d+1}$. The control points for the NURBS geometry are found by performing exactly the same projective transformation to the control points of the B-spline curve.

More about B-splines and NURBS in an isogeometric analysis setting can be found in [25].

3.1.2. LR B-splines. LR B-splines were proposed to overcome the limitation of B-splines and NURBS with respect to local refinement. B-splines and NURBS are formulated as tensor products of univariate B-splines and thus refinement in one of the univariate B-splines will cause the insertion of an entire new row or column of knots in the bivariate spline space. LR B-splines were first used in (adaptive) isogeometric analysis by [22].

For a short description of LR B-splines, local knot vectors are defined first. A given knot vector Ξ can be used to construct i local knot vectors Ξ_i, from the components of the original knot vector. A single B-spline of degree p may then be defined, using local knot vectors, as a separable function defined by n nondecreasing local knot vectors Ξ_i and the degrees p_i:

$$B_\Xi(\xi) = \prod_{i=1}^{n} B_{\Xi_i}(\xi_i) \tag{12}$$

To ensure that LR B-splines maintain the partition of unity property, a scalar weight $\gamma \in [0, 1]$ is introduced to define a weighted B-spline as

$$B_\Xi^\gamma(\xi) = \gamma \prod_{i=1}^{n} B_{\Xi_i}(\xi_i) \tag{13}$$

Next, we define box mesh, tensor mesh and LR mesh. A box mesh is a partitioning of a two-dimensional rectangular domain into smaller rectangles by horizontal and vertical lines. A tensor mesh is a box mesh where there are no T-joints, i.e., all horizontal and vertical lines span the entire length. An LR mesh $\mathcal{M}_n$ is a box mesh which results from a series of single line insertions from an initial tensor mesh $\mathcal{M}_0$ and each intermediate mesh is also a box mesh. A box mesh, tensor mesh or LR mesh with *multiplicities* is a mesh where each line segment has a corresponding integer value n, called the line multiplicity. Each multiplicity must satisfy $0 < n \leq p$, where p is the polynomial degree. These mesh types are illustrated in Figures 1a,1b and 1c.

The *support* of a (weighted) B-spline $B(\xi, \eta) = \gamma B_\Xi(\xi)B_\mathcal{H}(\eta)$ is the closure of all points where it takes nonzero value, where $\Xi = \{\xi_0, \xi_1, ..., \xi_{p_1+1}\}$, and $\mathcal{H} = \{\eta_0, \eta_1, ..., \eta_{p_1+1}\}$. A weighted B-spline has *minimal support* on an LR Mesh $\mathcal{M}$ if for every horizontal and vertical line of multiplicity n in the mesh $\mathcal{M}$ that traverses the support of the B-spline, there exist unique knot(s) corresponding to the lines depending on whether the lines traverse the interior or the edge of the B-spline.

We can now define LR B-splines based on the terminologies presented earlier. For a given LR Mesh $\mathcal{M}$, a function B is called an *LR B-spline* on $\mathcal{M}$ if $B_\Xi^\gamma(\xi) = \gamma B_\Xi(\xi)B_\mathcal{H}(\eta)$ is a weighted

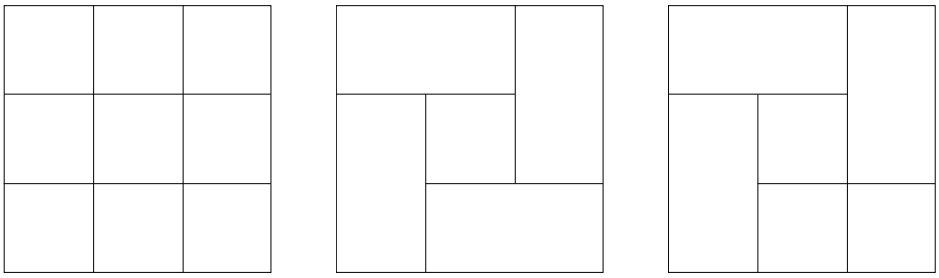

(a) Tensor mesh (b) Box mesh (c) LR mesh

Figure 1. Mesh types, after [22]

B-spline where all knot lines (and the knot line multiplicities) in Ξ and $\mathcal{H}$ are also in $\mathcal{M}$, and B has a minimal support on $\mathcal{M}$.

A given B-spline basis can be enriched by knot insertion without changing the geometric description. To insert a knot $\hat{\xi}$ into the knot vector Ξ between the knots ξ_{i-1} and ξ_i, we use the relation:

$$B_{\Xi}(\xi) = \alpha_1 B_{\Xi_1}(\xi) + \alpha_2 B_{\Xi_2}(\xi) \tag{14}$$

where

$$\begin{aligned} \alpha_1 &= \begin{cases} 1, & \xi_{p+1} \le \hat{\xi} \le \xi_{p+2} \\ \frac{\hat{\xi}-\xi_1}{\xi_{p+1}-\xi_1}, & \xi_1 \le \hat{\xi} \le \xi_{p+1} \end{cases} \\ \alpha_2 &= \begin{cases} \frac{\xi_{p+2}-\hat{\xi}}{\xi_{p+2}-\xi_2}, & \xi_2 \le \hat{\xi} \le \xi_{p+2} \\ 1, & \xi_1 \le \hat{\xi} \le \xi_2 \end{cases} \end{aligned} \tag{15}$$

and the knot vectors are

$$\begin{aligned} \Xi &= [\xi_1, \xi_2, ..., \xi_{i-1}, \quad \xi_i, ..., \xi_{p+1}, \xi_{p+2}] \\ \Xi_1 &= [\xi_1, \xi_2, ..., \xi_{i-1}, \hat{\boldsymbol{\xi}}, \xi_i, ..., \xi_{p+1} \quad\quad] \\ \Xi_2 &= [\quad \xi_2, ..., \xi_{i-1}, \hat{\boldsymbol{\xi}}, \xi_i, ..., \xi_{p+1}, \xi_{p+2}] \end{aligned} \tag{16}$$

The insertion of the knot $\hat{\xi}$ into Ξ yields a knot vector of size $p+3$, generating two B-splines described by the local knot vectors Ξ_1 and Ξ_2, both of size $p+2$.

Refinement by knot insertion using the above technique is illustrated on the B-splines given by the local knot vectors $\Xi_2 = [0,0,1,2]$, $\Xi_3 = [0,1,2,3]$ and $\Xi_4 = [1,2,3,3]$, all derived from the knot vector $\Xi = [0,0,0,1,2,3,3,4,4,4]$. For example, if we want to insert $\hat{\xi} = 3/2$ into the knot vector Ξ_3 between knots $\xi_2 = 1$ and $\xi_3 = 2$, this implies values of $\alpha_1 = \alpha_2 = 3/4$ and the resulting split is shown in Figure 2b. Similarly, the resulting B-spline splits when inserting $\hat{\xi} = 3/2$ in Ξ_2 and Ξ_4 are shown in Figure 2a and 2c.

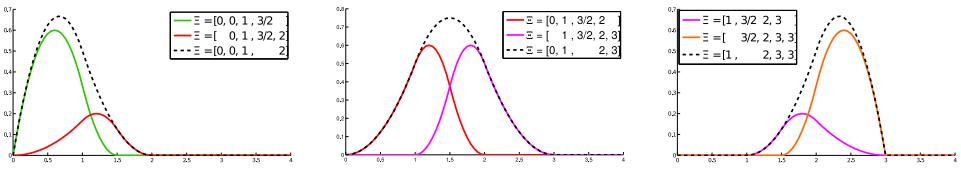

(a) Split of Ξ_2 (b) Split of Ξ_3 (c) Split of Ξ_4

Figure 2. Knot insertion example for LR B-splines, after [22]

Bivariate functions are refined in one parametric domain at a time. If we have a knot vector Ξ in the first parametric direction, and $\mathcal{H}$ in the second, we get a B-spline $B_{\Xi,\mathcal{H}}(\xi,\eta) = B_{\Xi}(\xi)B_{\mathcal{H}}(\eta)$.

Splitting in one direction is achieved by:

$$\begin{aligned} B_{\Xi}(\xi,\eta) &= B_{\Xi}(\xi)B_{\mathcal{H}}(\eta) \\ &= \left(\alpha_1 B_{\Xi_1}(\xi) + \alpha_2 B_{\Xi_2}(\xi)\right) B_{\mathcal{H}}(\eta) \\ &= \alpha_1 B_{\Xi_1}(\xi,\eta) + \alpha_2 B_{\Xi_2}(\xi,\eta) \end{aligned} \tag{17}$$

For a weighted B-spline, we have:

$$\begin{aligned} B^{\gamma}_{\Xi}(\xi,\eta) &= \gamma B_{\Xi}(\xi)B_{\mathcal{H}}(\eta) \\ &= \gamma\left(\alpha_1 B_{\Xi_1}(\xi) + \alpha_2 B_{\Xi_2}(\xi)\right) B_{\mathcal{H}}(\eta) \\ &= B^{\gamma_1}_{\Xi_1}(\xi,\eta) + B^{\gamma_2}_{\Xi_2}(\xi,\eta) \end{aligned} \tag{18}$$

where $\gamma_1 = \alpha_1\gamma$ and $\gamma_2 = \alpha_2\gamma$.

LR B-splines form a partition of unity, i.e.,

$$\sum_{i=1}^{n} \gamma_i B_i(\xi) = 1 \tag{19}$$

To control adaptive refinement in isogeometric analysis with LR B-splines, we introduce a refinement parameter β. The refinement parameter β is defined such that two LR B-splines $\mathcal{L}_{i-1}$ and $\mathcal{L}_i$ satisfy

$$\mathcal{L}_{i-1} \subset \mathcal{L}_i \qquad \text{and} \qquad (1+\beta)|\mathcal{L}_{i-1}| \leq |\mathcal{L}_i| \tag{20}$$

which states that $\mathcal{L}_i$ should be a refinement of $\mathcal{L}_{i-1}$ and the number of B-splines should grow by at least β percent during each iteration. Thus, β in this case represents the growth rate of the number of basis functions in the solution space i.e. if we have n degrees of freedom at refinement step i, we will have, at least, $n \times (1 + \beta/100)$ degrees of freedom at refinement step $i + 1$. We could also choose β to represent the percentage of elements with the largest error contribution to be refined. For the numerical examples in this paper, β refers to the growth rate of the basis functions. The value of β in a simulation is selected such that the adaptive simulation is as efficient and as accurate as possible. Smaller values for β result in a more accurate adaptive refinement while larger values reduce the number of refinement steps, and thereby the computation time. Typical values are in the range $5\% \leq \beta \leq 20\%$, [22].

3.2. Variational formulation

In this section, we present the weak formulation of the governing equation. Our aim is to solve the equation:

$$\nabla \cdot \left[-\frac{1}{\gamma^w}\mathbf{k}\left(\nabla p^w - \rho^w \mathbf{g}\right)\right] = f$$

for the pressure p^w with the boundary conditions given in Eq. 7. Applying a differentiable test function v to the previous equation and integrating over the domain Ω, we get:

$$\int_{\Omega} v\, \nabla \cdot \left[-\frac{1}{\gamma^w}\mathbf{k}\left(\nabla p^w - \rho^w \mathbf{g}\right)\right] \mathrm{d}\Omega = \int_{\Omega} f v \,\mathrm{d}\Omega \tag{21}$$

Applying Green's theorem to the integrand with the divergence operator and choosing appropriate test functions, we can write a proper statement of the weak form as: Find $p^w \in V$ such that

$$a(p^w, v) = L(v) \qquad \forall v \in \hat{V} \tag{22}$$

where

$$\begin{aligned} a(p^w, v) &= \int_{\Omega} \nabla v \cdot \frac{1}{\gamma^w}\mathbf{k} \cdot \nabla p^w \,\mathrm{d}\Omega \\ L(v) &= \int_{\Omega} f v \,\mathrm{d}\Omega + \int_{\Omega} \nabla v \cdot \frac{1}{\gamma^w}\mathbf{k} \cdot \rho^w \mathbf{g} \,\mathrm{d}\Omega - \int_{\Gamma_N} q^w v \,\mathrm{d}\Gamma \end{aligned} \tag{23}$$

The trial and test spaces V and $\hat{V}$ are defined as:

$$\begin{aligned} V &= \left\{ v \in H^1(\Omega) : v = \hat{p}^w \quad \text{on} \quad \Gamma_D \right\} \\ \hat{V} &= \left\{ v \in H^1(\Omega) : v = 0 \quad \text{on} \quad \Gamma_D \right\} \end{aligned} \tag{24}$$

3.3. Galerkin finite element formulation

The finite element approximation corresponding to the variational formulation given in Eq. 22 reads: Find $p_h^w \in V_h$ such that

$$a(p_h^w, v_h) = L(v_h) \qquad \forall v_h \in \hat{V}_h \tag{25}$$

where p_h^w is the FE approximation to the pressure field, v_h is the FE test function, and for compatible FE trial and test spaces we have $V_h \subset V$ and $\hat{V}_h \subset \hat{V}$, respectively. Notice that the dimensions for $\hat{V}$ and V are infinite, whereas the dimensions for $\hat{V}_h$ and V_h are finite (i.e. equal to the number of FE basis functions).

The FE pressure may be written as a linear combination of the FE basis functions $\mathbf{N}$ and the nodal values (control point values in IGA) $\bar{\mathbf{p}}^w$ as:

$$p_h^w = \mathbf{N}\bar{\mathbf{p}}^w \tag{26}$$

Applying Galerkin's method, the test functions in the weak form are chosen to be the same as the shape functions (after the non-homogeneous Dirichlet boundary conditions are taken care of, i.e. their effect is moved to the right hand side). Thus, when applied to the weak form in Eq. 22, this results in the linear matrix equation:

$$\mathbf{A}\bar{\mathbf{p}}^w = \mathbf{b} \tag{27}$$

where

$$\begin{aligned} \mathbf{A} &= \int_\Omega (\nabla \mathbf{N})^T \frac{1}{\gamma^w} \mathbf{k} \, (\nabla \mathbf{N}) \mathrm{d}\Omega \\ \mathbf{b} &= \int_\Omega \mathbf{N} f \mathrm{d}\Omega + \int_\Omega (\nabla \mathbf{N})^T \frac{1}{\gamma^w} \mathbf{k} \, \rho^w \mathbf{g} \mathrm{d}\Omega - \int_{\Gamma_N} \mathbf{N} q^w \mathrm{d}\Gamma \end{aligned} \tag{28}$$

4. ERROR ESTIMATES AND ADAPTIVITY

4.1. Introduction

In this section, we discuss the procedures for calculating a posteriori error estimates based on recovery of the computed solution. The adaptive mesh refinement strategies based on the error criteria are also discussed.

Since the 1970s several strategies have been developed to estimate the discretization error of a Finite Element (FE) solution. Babuska and Rheinboldt presented the pioneering effort in this regard back in 1978, see [26], [27]. Since then many different estimation procedures have been introduced; see [28] for an overview. A popular class of error estimators denoted *recovery based estimators* consist of deriving a simple smoothing technique that yields a solution field or, more commonly, the gradient of the solution, that converges faster than the FE solution or its gradient, respectively. A very popular prototype for such approaches is the Zienkiewicz-Zhu error estimate (so called ZZ estimate). Initial reference to such estimates can be found in [29], and further development with *Superconvergent Patch Recovery* (SPR) in [30], [31]. The success of this approach in the engineering community relies on an intuitive mechanical definition and a certain ease of implementation compared to other class of available error estimates, without sacrificing the numerical effectivity.

The second author of this paper has more than two decades of experience in developing and implementing a posteriori error estimators. First, in [32] and [33], we extended the SPR-procedure by recovering statically admissible stress fields for plane stress and Reissner-Mindlin plates, respectively. Then, goal oriented recovery of stresses in elasticity, and surface forces (drag and lift) for Stokes problems were developed and presented in the papers [34], [35] and [36], respectively.

Object oriented implementation of the SPR-recovery procedures is described in [37] and [38]. Recently, we have developed a posteriori error estimates for isogeometric analysis, see [39] and [40]. The first paper gives an extensive study of different recovery based error estimators. Furthermore, it presents, for the first time, a true *superconvergent* patch recovery method for adaptive isogeometric analysis using LR B-splines.

Our main aim with the present paper is to show the possibilities that open up with adaptive IGA using LR B-splines. An open-source package for using LR B-splines may be downloaded at http://lrbsplines.com/. However, anyone who wants to perform adaptive IGA using LR B-splines will have to implement an algorithm for a posteriori error estimation. Based on the experiences mentioned above we have chosen herein to use a simple a posteriori error estimator, the Continuous Global L_2 (CGL2) projection, as first presented in [29] for FE and in [40] for IGA, as it gives reasonably good results and is easy to implement.

4.2. A priori error estimates

Let p^w and p_h^w represent the exact and isogeometric finite element solutions, respectively. The discretization error in the pressure, e, and the error in the pressure gradient, e_σ, are defined as:

$$\begin{aligned} e &:= p^w - p_h^w \\ e_\sigma &:= \nabla p^w - \nabla p_h^w \end{aligned} \tag{29}$$

Introducing the error norms in L_2 corresponding to e and e_σ:

$$\begin{aligned} \|e\|_{L^2(\Omega)} &:= \|p^w - p_h^w\|_{L^2(\Omega)} = \left(\int_\Omega (p^w - p_h^w)^2 \, \mathrm{d}\Omega \right)^{1/2} \\ \|e_\sigma\|_{L^2(\Omega)} &:= \|\nabla p^w - \nabla p_h^w\|_{L^2(\Omega)} = \left(\int_\Omega (\nabla p^w - \nabla p_h^w)^T (\nabla p^w - \nabla p_h^w) \, \mathrm{d}\Omega \right)^{1/2} \end{aligned} \tag{30}$$

Steady-state groundwater flow is a self-adjoint problem and it follows that the computed FE-solution is optimal in energy norm. The energy norm using the bilinear form from Section 3.2 is given by (which is equivalent to seminorm of error e on $H_0^1(\Omega)$):

$$\|e\|_E = \sqrt{a(e,e)} = |e|_{H_0^1(\Omega)} \tag{31}$$

which is the same as:

$$\|e\|_E = \left(\int_\Omega (\nabla p^w - \nabla p_h^w)^T \frac{1}{\gamma^w} \mathbf{k} (\nabla p^w - \nabla p_h^w) \, \mathrm{d}\Omega \right)^{1/2} \tag{32}$$

If the analytical solution of a variational problem involving first order differentiation (as is the case herein) is sufficiently smooth, i.e. $p^w \in H^{p+1}$, and the FE mesh $\mathcal{M}_0$ is regular and quasi-uniform, the error in the approximate FE-solution on a family of uniformly refined meshes $\{\mathcal{M}_k\}$, is bounded by

$$\|p^w - p_h^w\|_E = C h^p \|p^w\|_{H^{p+1}} \tag{33}$$

where C is some problem-dependent constant, h is the characteristic size of the finite elements, p is the degree of the largest complete polynomial in the FE basis functions and $||p^w||_{H^{p+1}}$ denotes the Sobolev norm of order $p+1$.

For problems where the solution is not sufficiently smooth, $p^w \notin H^{p+1}$, e.g. problems with singular points within the solution domain or on its boundary, we have the error bound

$$\|p^w - p_h^w\|_E = C h^\alpha \|p^w\|_{H^{\alpha+1}} \tag{34}$$

where the value of the non-negative real parameter α depends on how the family of meshes $\{\mathcal{M}_k\}$ are created.[†] Assume that λ is a real number characterizing the strength of the singularity. For a

[†]As α is not necessarily an integer, $\|p^w\|_{H^{\alpha+1}}$ is a *a Sloboditskii* norm.

sequence of uniformly, or nearly uniformly, refined meshes we then have

$$\alpha = \min\{p, \lambda\}. \tag{35}$$

Thus, when $\lambda < p$ the rate of convergence is limited by the strength of the singularity and not the polynomial order.

4.3. A posteriori error estimates

The a priori error estimates do not give any quantification of the error for a simulation with a given mesh and a spline space; we only get information about the expected convergence rate. However, in order to perform an adaptive refinement, we need to quantify the error distribution throughout the mesh, i.e. on each element. For this we use *a posteriori error estimates* that in one way or another are based on the computed FE solution p_h^w. A popular approach for a posteriori error estimation is based on postprocessing the gradients of the finite element computed pressure solution, as the finite element computed pressure gradient, ∇p_h^w, can be improved by global projection or local smoothing.

As mentioned above, we use herein Continuous Global L^2 (CGL2) projection to obtain the improved gradients ∇p_r^w. The improved convergence rate for ∇p_r^w is due to *superconvergent* that has been proven under certain conditions of the regularity of the solution and the mesh topology by [41], both for C^0 finite elements and C^{p-1} splines. We aim to obtain an improved pressure gradient field:

$$\nabla p_r^w = \mathbf{N}\mathbf{a}_r \tag{36}$$

where $\mathbf{N}$ are the shape functions for the pressure, see Eq. 26, and $\mathbf{a}_r$ is the unknown vector of new control variables determining the recovered pressure gradient ∇p_r^w. Notice that the computed pressure gradient reads

$$\nabla p_h^w = \nabla \mathbf{N}\mathbf{p}^w \tag{37}$$

i.e. we are aiming to recover a pressure gradient ∇p_r^w in a one polynomial order higher spline space than the computed pressure gradient ∇p_h^w.

The vector of control variables $\mathbf{a}_r$ are determined by forcing a least square fit (i.e. global L_2 projection) of ∇p_r^w to the computed FE pressure gradient ∇p_h^w, i.e.

$$\mathcal{J}(\mathbf{a}_r) = \int_\Omega (\nabla p_r^w - \nabla p_h^w)^T \cdot (\nabla p_r^w - \nabla p_h^w)\, \mathrm{d}\Omega \tag{38}$$

is minimized with respect to $\mathbf{a}_r$. The minimization

$$\frac{\partial \mathcal{J}}{\partial \mathbf{a}_r} = 2 \int_\Omega \left(\frac{\partial \nabla p_r^w}{\partial \mathbf{a}_r} \right)^T \cdot (\nabla p_r^w - \nabla p_h^w)\, \mathrm{d}\Omega \tag{39}$$

yields a linear system of equations given by

$$\mathbf{A}\mathbf{a}_r = \mathbf{b}_r \tag{40}$$

where

$$\mathbf{A} = \int_\Omega \mathbf{N}^T \mathbf{N} \mathrm{d}\Omega \qquad \text{and} \qquad \mathbf{b}_r = \int_\Omega \mathbf{N}^T \nabla p_h^w \mathrm{d}\Omega \tag{41}$$

We now use the improved gradients to get an indication of the error in the computed pressure:

$$e_{\sigma_r} := \nabla p_r^w - \nabla p_h^w \tag{42}$$

The corresponding energy norm associated with the bilinear form is:

$$\|e_r\|_E = \left(\int_\Omega (\nabla p_r^w - \nabla p_h^w) \cdot \frac{1}{\gamma^w} \mathbf{k} \cdot (\nabla p_r^w - \nabla p_h^w)\, \mathrm{d}\Omega \right)^{1/2} \tag{43}$$

The quality of the error estimate based on improved gradients is measured by its effectivity index, which is defined as the ratio of the estimated error to the actual error:

$$\theta = \frac{\|e_r\|_{E(\Omega)}}{\|e\|_{E(\Omega)}} \tag{44}$$

The relative global error (in percentage) is a dimensionless error quantity defined for exact and recovered error estimates, respectively, as:

$$\rho = \frac{\|e\|_E}{\|p^w\|_E} \times 100\% \quad \text{and} \quad \rho_r = \frac{\|e_r\|_E}{\|p_r^w\|_E} \times 100\% \tag{45}$$

where $\|p^w\|_E = \sqrt{a(p^w, p^w)}$ and $\|p_r^w\|_E = \sqrt{a(p_r^w, p_r^w)}$ are the energy norms of the exact and L_2-projected solutions, respectively.

4.4. Adaptive refinement

Once a posteriori error estimates are established, the elements that require refinements are identified based on a tolerance criteria. The next step is to locally refine the elements. For a linear two dimensional element or knotspan that requires refinements, knot insertion splits that element into four new elements. However, for B-splines of higher polynomial order, $p > 1$, the splitting cross cannot be limited to only the element in question. Thus, local refinement strategies must be selected to have the desired refinement for a given element and its neighbors. We have three local refinement strategies for LR B-splines, namely *full span*, *minimum span* and *structured mesh* refinement. The ideas behind these strategies are briefly discussed here and for the details we refer to [22].

The full span refinement strategy refines every B-spline with support on the element identified for refinement. The mesh line inserted in one direction will span from the minimum to the maximum knot of all functions with support on the identified element. This strategy ensures that all B-splines with support on the identified element are split by the refinement. This approach is illustrated in Figure 3a.

In the minimum span refinement strategy, a cross is inserted in the identified element where the refinement footprint is limited, unlike the full span approach. The inserted mesh lines will be as short as possible but will split at least one B-spline. The B-spline to be split maybe identified based on which of the available B-splines has the smallest parametric support. But, in general, there is lack of such uniqueness. Thus, a random B-spline is selected and refined. This approach is shown in Figure 3b.

Identifying which B-splines need refinement instead of which elements is another way to refine B-splines. In [22] the error for a B-spline is defined as the sum of the errors in all the knotspans in the support of the given B-spline. A fraction of the B-splines with the highest error are then refined as illustrated in Figure 3c resulting in a structured mesh refinement.

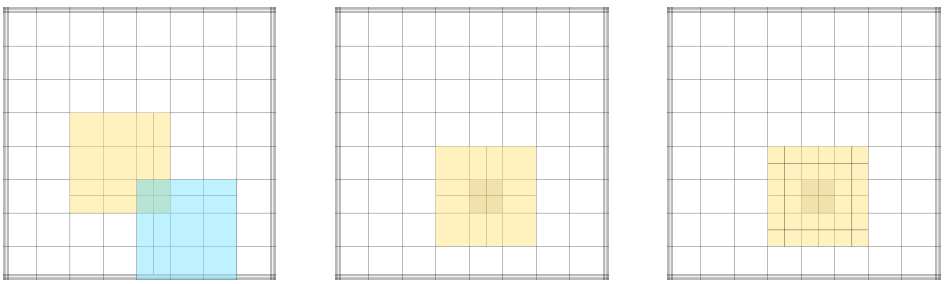

(a) Fullspan: Split all functions on one element (b) Min Span: Split one random function on one element (c) Structured Mesh: Split all knot spans on one B-spline

Figure 3. Local refinement strategies for LR B-splines, after [22]

5. NUMERICAL EXAMPLES

5.1. Aims of the numerical examples

The aim of the numerical experiments herein is to investigate whether adaptive refinement using LR B-splines achieves optimal convergence rates for groundwater flow problems that may involve highly varying material properties, singularities and/or rough right hand sides such that it gives better accuracy per number of degrees of freedom compared to uniform refinement. The adaptive strategy is based on controlling the growth rate of the basis functions in the solution space, according to the parameter β, and a specified error tolerance or maximum number of degrees of freedom. Furthermore, we want to investigate the sensitivity in accuracy and convergence rates towards polynomial order p. We start the numerical examples with two verification problems with known analytical solutions:

- The wavefront well problem
- The L-shape problem

These problems are used to verify the numerical implementation and study the effectivity of the error estimates and the adaptive simulation in handling certain challenging effects. In the wavefront well problem we study the effects of a rough right hand side and the effect of isotropy/anisotropy in material properties, whereas the analytical solution for the L-shape problem is characterized by having a singularity of the gradient in the re-entrant corner on the boundary. The availability of an analytical solution allows us to calculate exact a posteriori error estimates to drive the adaptive mesh refinement, as well as study and report the effectivity index for the presented recovery based error estimator.

To demonstrate the potential offered by adaptive isogeometric analysis, we address the following groundwater flow problems:

- Flow around an impervious corner
- Flow around a cutoff wall
- Flow in a heterogeneous medium

Analytical solutions are not available for these problems and we use the a posteriori error estimator to drive the adaptive refinement. Here we compare the achieved accuracy per number of degrees of freedom, $ndof$, obtained with adaptive and uniform refinement.

5.2. Verification problems with analytical solutions

5.2.1. The wavefront well problem. The first illustrative example we consider is the so called wavefront well problem, [42], defined over a square domain.

Problem definition. The strong form of the problem in Eq. 7, assuming the flow is solely driven by pressure gradients, reduces to:

$$\begin{cases} \nabla \cdot [-\boldsymbol{\kappa} \nabla p^w(x,y)] = f(x,y) & (x,y) \in \Omega \\ p^w(x,y) = \hat{p}^w(x,y) & (x,y) \in \partial\Omega \end{cases} \tag{46}$$

The numerical simulation domain is defined by a square area $\Omega = [0,1] \times [0,1]$ where the boundaries are $\Gamma_D = \partial\Omega$ and $\Gamma_N = \varnothing$, shown in Figure 4a. The exact analytical solution for the pressure field is given by:

$$p^w(x,y) = \arctan(50(-0.25 + \sqrt{(x-0.5)^2 + (y-0.5)^2})) \tag{47}$$

Note that the right hand side $f(x,y)$ is generated by taking the Laplacian (∇^2) of the analytical solution stated in Equation 47, and is given in Appendix A for a variable degree of anisotropy. The analytical solution depicted in Figure 4b displays a "front"-type of behavior where the solution is rapidly changing across a circular band inside the domain. This problem is mathematically smooth

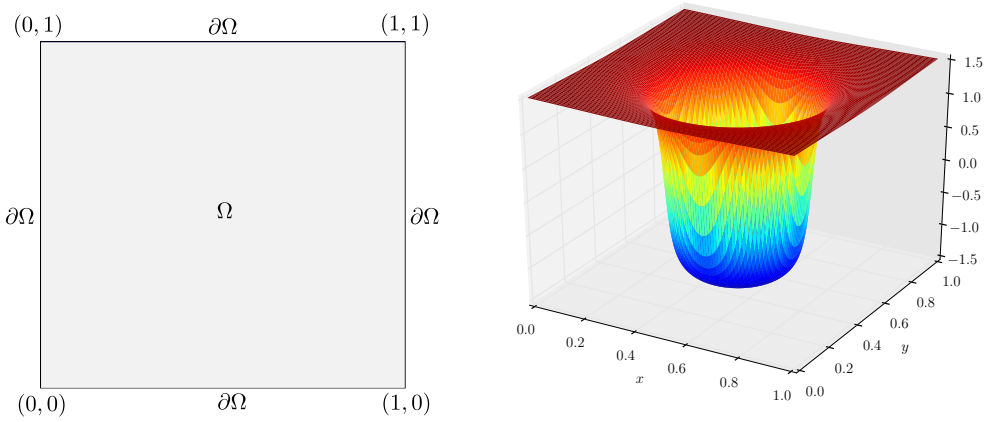

(a) The domain Ω and its boundary

(b) 3D plot of analytical solution

Figure 4. **The wavefront problem**: Numerical simulation domain and analytical solution plot

i.e. $p^w \in H^{p+1}(\Omega)$ for any finite p. However, due to the highly varying right hand side we may only expect an optimal convergence rate when the element size h is less than a given threshold that depends on the sharpness/bandwidth of the interior layer. Hence, we may expect suboptimal convergence rate for uniform mesh refinement when the mesh is not fine enough.

Two cases are considered for the conductivity matrix $\boldsymbol{\kappa}$ - isotropic and anisotropic. For simplicity in deriving the source function, the conductivity equivalent coefficients are set equal to:

$$\boldsymbol{\kappa} = \begin{bmatrix} 1 & 0 \\ 0 & 1 \end{bmatrix} \quad \text{and} \quad \boldsymbol{\kappa} = \begin{bmatrix} 10 & 0 \\ 0 & 1 \end{bmatrix} \tag{48}$$

Results - isotropic case. The adaptive simulation is performed for polynomial degrees of $p = 2$ and $p = 3$. The refinement parameter is selected as $\beta = 20\%$. Adaptive refinement is performed upto a specified maximum number of iterations or maximum number of degrees of freedom.

The physical meshes for selected refinement steps are shown in Figures 5a-5c for $p = 2$ and in Figures 5d-5f for $p = 3$. The structured mesh refinement strategy is used for this problem. Note that the adaptive meshes are not perfectly symmetric, even though the solution and error distribution are symmetric, because our refinement parameter β only controls the growth rate of the number of basis functions, as explained in Section 3.1.2. We observe, however, that the physical meshes especially at higher refinement steps are nearly symmetric since the error is symmetrically distributed because of its dependence on the hydraulic conductivity matrix.

The convergence plots for this case are shown in Figure 6a in terms of relative error versus number of degrees of freedom. The effectivity index plot is shown in Figure 6b for the polynomial degrees considered. It can bee seen from the curves that an optimal convergence rate is obtained after a sufficient number of refinements for this problem. A similar problem has been studied in [40] using different a posteriori error estimators, of which CGL2 (used here) is one. Error recovery based on CGL2 projection was observed to perform well for this problem.

Results - anisotropic case. The problem is simulated with the same setup as in the isotropic case with the only difference being in the anisotropy of the $\boldsymbol{\kappa}$ matrix. The errors are no longer symmetrically distributed in the domain and this is reflected in the physical meshes obtained at different refinements steps, shown in Figures 7a-7c for $p = 2$ and Figures 7d-7f for $p = 3$. The convergence plots obtained for the anisotropic case, Figure 8a, are similar to the isotropic case. The effectivity index plot for this case is shown in Figure 8b.

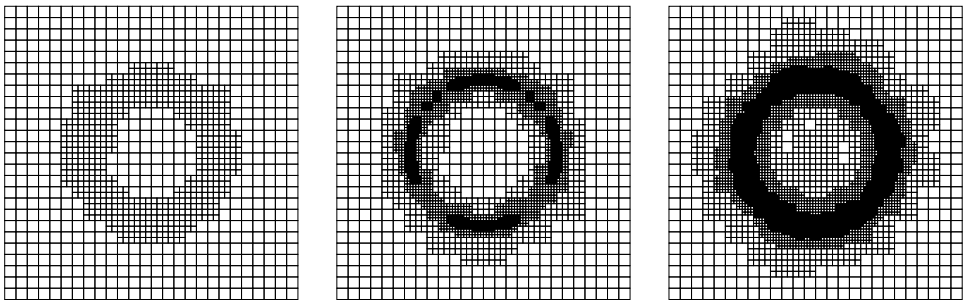

(a) $p = 2$, $ndof = 1138$ (b) $p = 2$, $ndof = 3443$ (c) $p = 2$, $ndof = 10339$

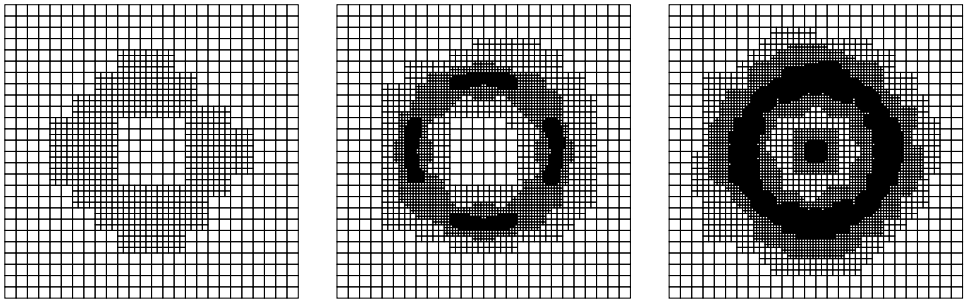

(d) $p = 3$, $ndof = 1234$ (e) $p = 3$, $ndof = 3775$ (f) $p = 3$, $ndof = 11320$

Figure 5. **The wavefront problem**: Adaptive meshes for $\beta = 20\%$ at different refinement steps for the isotropic case. Each column represents the same refinement step for varying polynomial degrees.

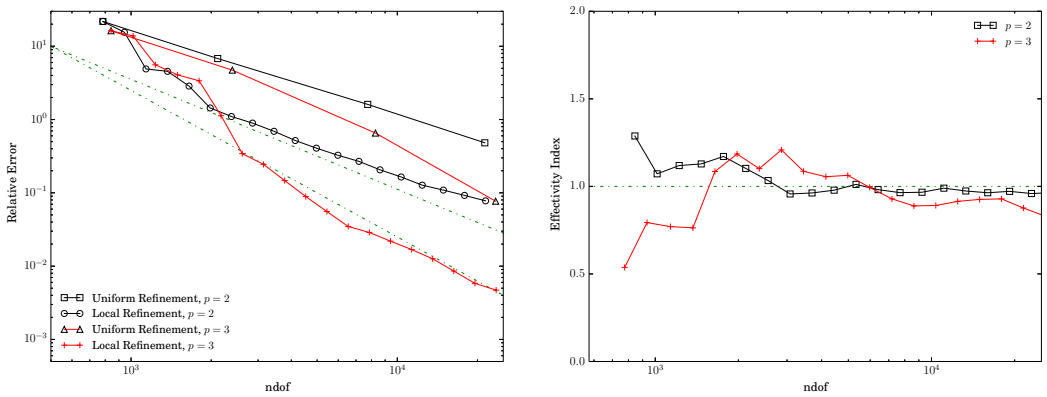

(a) (b)

Figure 6. **The wavefront problem**: Convergence and effectivity index plots for the isotropic case. The dotted lines in a) correspond to slopes of -3/2 and -2.

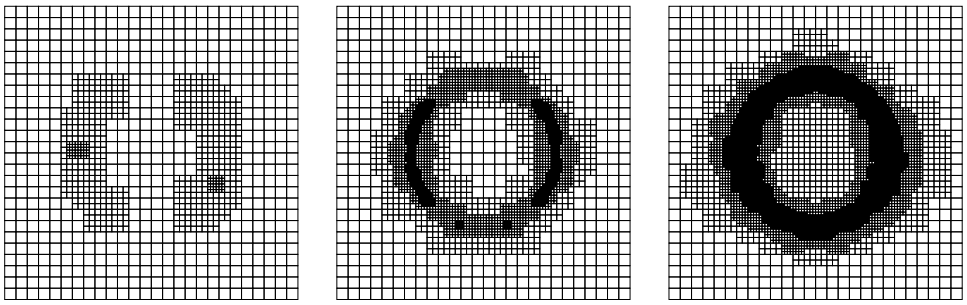

(a) $p = 2$, $ndof = 1135$ (b) $p = 2$, $ndof = 3443$ (c) $p = 2$, $ndof = 10352$

(d) $p = 3$, $ndof = 1222$ (e) $p = 3$, $ndof = 3751$ (f) $p = 3$, $ndof = 11230$

Figure 7. **The wavefront problem**: Adaptive meshes for $\beta = 20\%$ at different refinement steps for the anisotropic case. Each column represents the same refinement step for varying polynomial degrees.

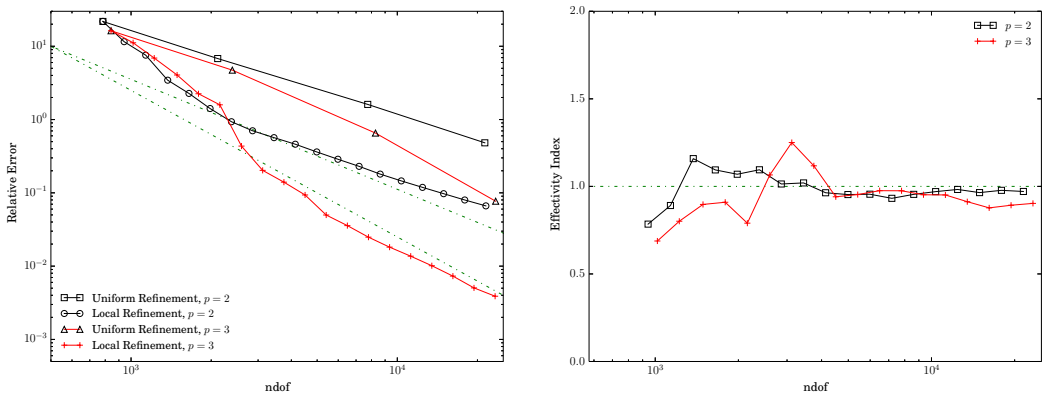

(a) (b)

Figure 8. **The wavefront problem**: Convergence and effectivity index plots for the anisotropic case. The dotted lines in a) correspond to slopes of -3/2 and -2.

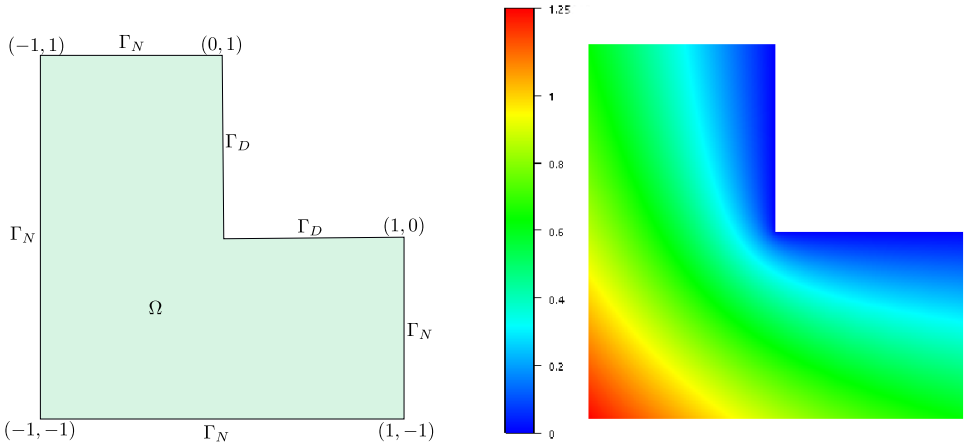

(a) Domain (b) Analytical solution

Figure 9. **The L-shape problem:** Domain with boundary conditions and analytical solution plot

5.2.2. The L-shape problem. The second example with analytical solution is the L-shape problem with domain and boundary conditions shown in Figure 9a.

Problem definition. The boundary conditions are summarized as:

$$\begin{cases} \nabla \cdot (-\boldsymbol{\kappa} \nabla p^w) = 0 & \text{in} \quad \Omega \\ p^w(r, \theta) = 0 & \text{on} \quad \Gamma_D \\ \frac{\partial p^w}{\partial n} = q^w & \text{on} \quad \Gamma_N \end{cases} \tag{49}$$

We choose $\kappa_x = \kappa_y = 1$ for simplicity. The exact analytical solution is given by:

$$p^w = r^{2/3} \sin\left(\frac{2\theta - \pi}{3}\right) \tag{50}$$

where $r^2 = x^2 + y^2$ and $\theta = \arctan(y/x)$. The analytical solution plot is shown in Figure 9b. The expression for the Neumann boundary condition, q^w, is derived based on the analytical solution and is not included here.

For the given elliptic problem, the re-entrant corner at $(0, 0)$ in the domain causes a singularity in the solution. It is known that the convergence for uniform mesh refinement is limited by the strength of the singularity $\lambda = 2/3$, as $p^w \in H^{5/3}(\Omega)$, i.e., the convergence rate (versus degrees of freedom) is equal to $-1/3$. For problems where the solution is not sufficiently smooth, $p^w \notin H^{p+1}(\Omega)$, we do not obtain an optimal convergence rate when we perform uniform mesh refinement. In particular, the use of higher order polynomials is then inefficient.

Results. The L-shape problem is analyzed for polynomial degrees of $p = 2$ and $p = 3$. The refinement parameter is selected as $\beta = 20\%$. In Figure 10a we see that we achieve optimal convergence rates when we perform adaptive refinement, whereas for uniform refinement the convergence rate is the same for both $p = 2$ and $p = 3$ and limited by the strength of the singularity. The effectivity index plots obtained are shown in Figure 10b and we see that we have $0.9 < \theta < 1.1$. We want to underline that the obtained effectivity indices are very good (i.e close to 1.0) compared to what we typically achieve for regular finite elements [32].

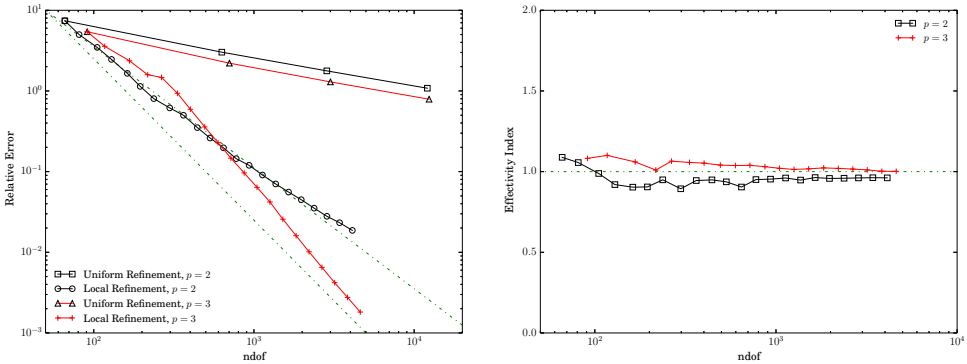

(a) (b)

Figure 10. **The L-shape problem**: Convergence and effectivity index plots

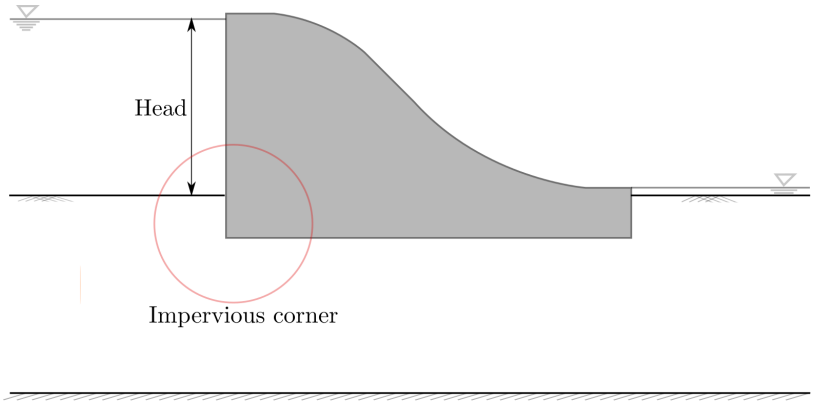

Figure 11. One example of seepage around an impervious corner

5.3. Flow around an impervious corner

The next numerical example we consider is flow of water around an impervious corner e.g. groundwater flow under the base of a concrete dam, Figure 11. The presence of a sharp corner introduces singularity in the numerical solution leading to infinite velocities.

5.3.1. Problem definition. We study a selected area of this problem with adaptive mesh refinement by considering the appropriate boundary conditions. The problem is idealized as an L-shape problem where the boundary conditions are applied such that they reflect the physical problem, shown in Figure 12a. Dirichlet boundary conditions are applied at the top horizontal and the right vertical edges of the idealized numerical simulation domain. For simplicity, a homogeneous Dirichlet boundary condition is applied at the right vertical edge, which may be slightly different in the the physical problem depending on the boundary conditions at the downstream area. The impervious boundary Γ_{N1} represents a homogeneous Neumann boundary condition. We assume the fluxes to be negligible on Γ_{N2}. The boundary conditions are summarized as:

$$\begin{cases} p^w = 1000 & \text{on} \quad \Gamma_{D1} \\ p^w = 0 & \text{on} \quad \Gamma_{D2} \\ \frac{\partial p^w}{\partial n} = 0 & \text{on} \quad \Gamma_{N1} \cup \Gamma_{N2} \end{cases} \tag{51}$$

The equipotential lines obtained from simulations with uniform refinement using coarse and fine meshes are shown in Figures 12b and 12c, respectively.

5.3.2. Results. The mesh refinement parameter for this problem is selected as $\beta = 20\%$ and the adaptive simulations are performed in combination with polynomial degrees of $p = 2$, $p = 3$ and $p = 4$. The fullspan refinement strategy is used in this case.

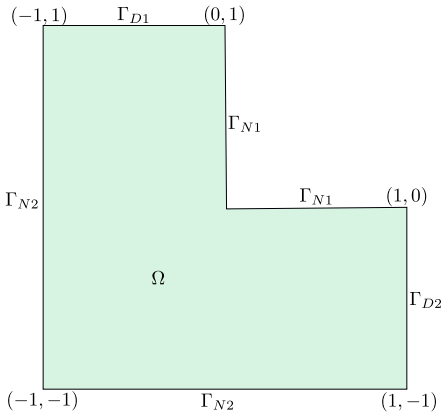

(a) Domain

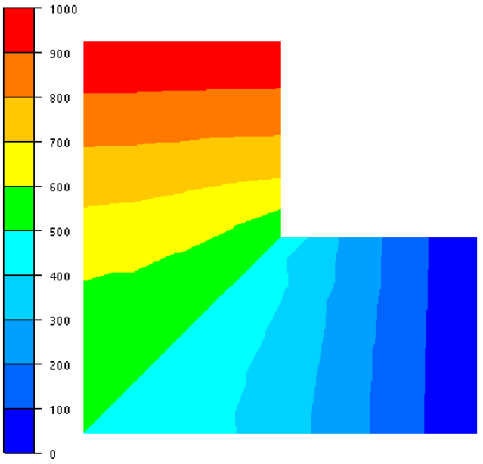

(b) Equipotential lines, $ndof = 66$

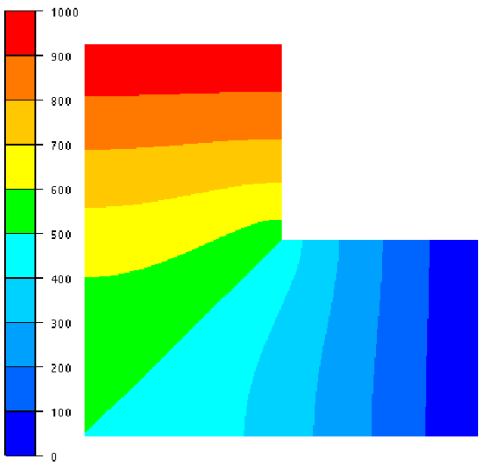

(c) Equipotential lines, $ndof = 3571$

Figure 12. **The impervious corner problem**: Idealized numerical simulation domain and equipotential lines for coarse and fine meshes.

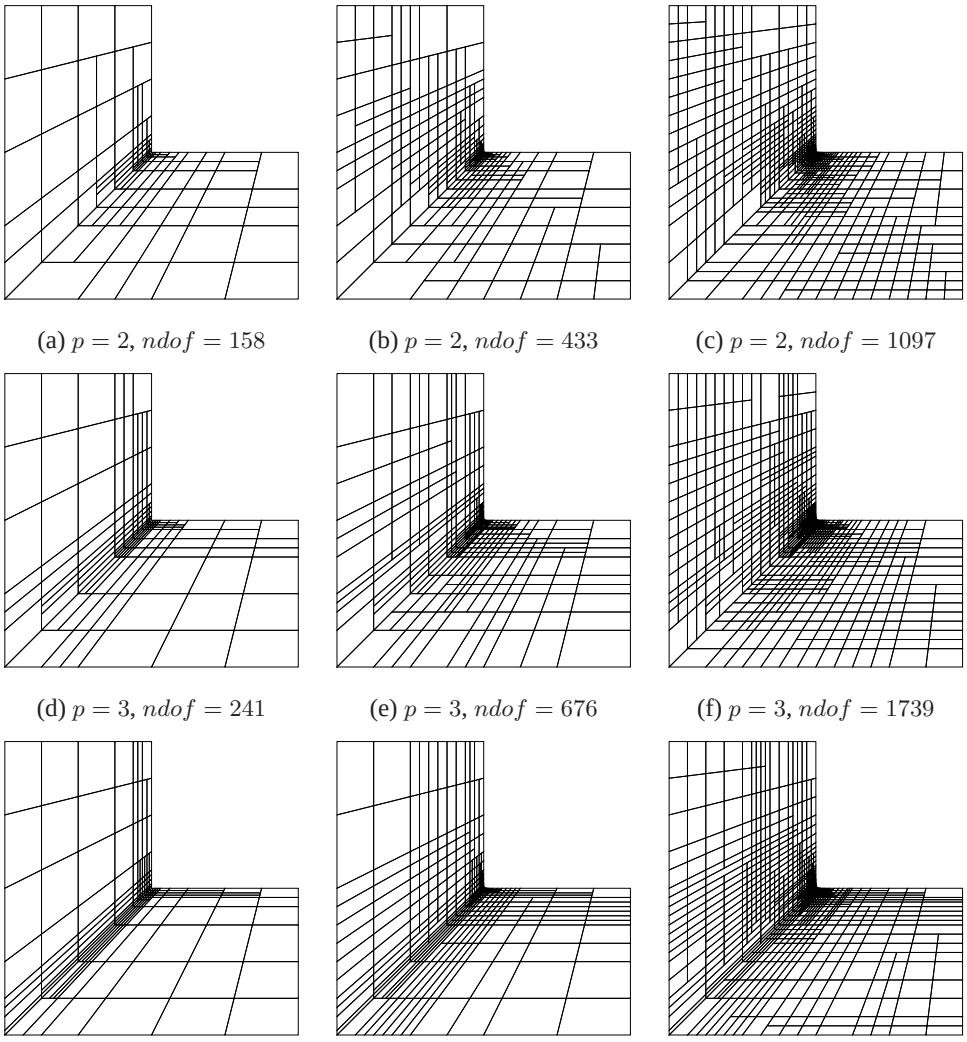

(a) $p = 2$, $ndof = 158$ (b) $p = 2$, $ndof = 433$ (c) $p = 2$, $ndof = 1097$

(d) $p = 3$, $ndof = 241$ (e) $p = 3$, $ndof = 676$ (f) $p = 3$, $ndof = 1739$

(g) $p = 4$, $ndof = 290$ (h) $p = 4$, $ndof = 807$ (i) $p = 4$, $ndof = 2068$

Figure 13. **The impervious corner problem**: Adaptive meshes at different refinement steps for the selected $\beta = 20\%$. Each column represents the same refinement step for varying polynomial degrees.

The resulting physical meshes at selected refinement steps are shown in Figure 13. The meshes and the resulting number degrees of freedom for $p = 2$ at the 5th, 10th and 15th refinement steps are shown in Figures 13a-13c. Similar results for $p = 3$ and $p = 4$ are shown in Figures 13d-13f and Figures 13g-13i, respectively. The convergence plots in Figure 14 compare the relative errors from simulations with local and uniform refinement for the different polynomial degrees analyzed. Observe the significant increase of convergence order, i.e. optimal convergence rate, achieved by the adaptive procedure. The convergence rate with local refinement in this case appears to improve with increasing polynomial order.

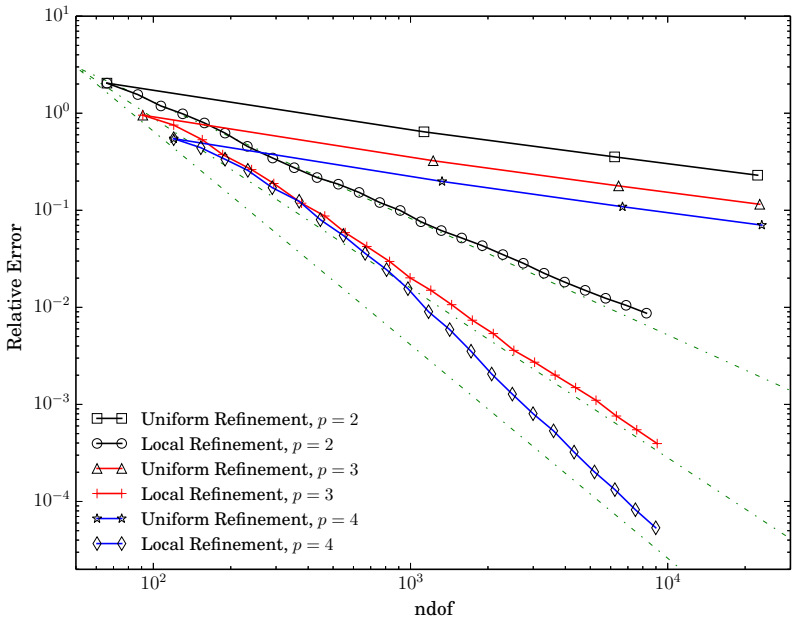

Figure 14. **The impervious corner problem**: Convergence plots

5.4. Flow around a cutoff wall

Seepage cutoff walls are used in geotechnical engineering to protect structure foundations from the damaging effects of groundwater flow or to exclude groundwater from an excavation and thereby minimize the requirement of dewatering pumping. The cutoff walls are usually made of an impervious or very low permeability material, such as a steel sheet-pile wall, and extend up to a zone of low permeability. In the computational modeling of groundwater flow, the tips of such cutoff walls represent points of singularity, [9], making the numerical solution difficult or erroneous.

5.4.1. Problem definition. We consider the flow of water around a 10m long cutoff wall installed under the base of a dam with a cross-sectional width of 50m, see Figure 15. The soil medium is considered to be homogeneous with an isotropic hydraulic conductivity of 15 m/day.

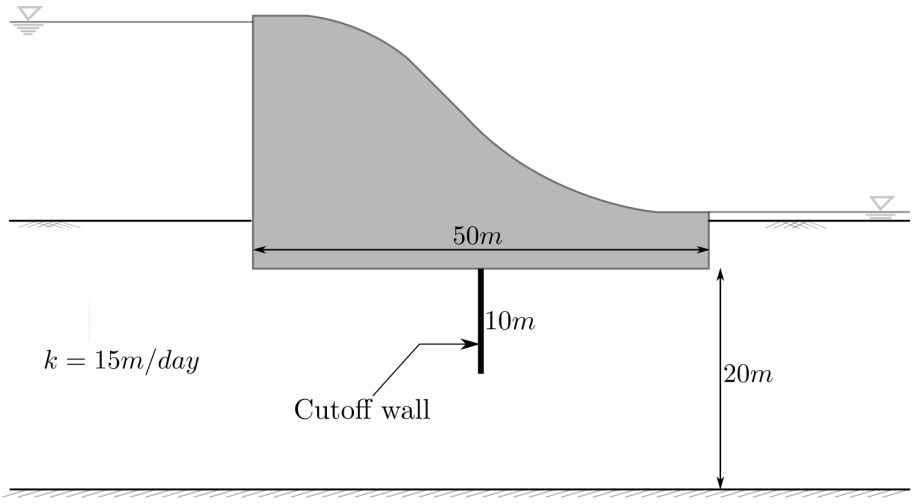

Figure 15. **The cutoff wall problem**: Physical setup of dam with a cutoff wall

The simulation domain chosen for the described dam with a cutoff wall is shown in Figure 16a. The cutoff wall is included in the geometry by inserting a C^{-1} discontinuous knot. The base of the dam, the cutoff wall and the boundary to the impervious layer represent homogeneous Neumann boundaries and are respectively designated as Γ_{N1}, Γ_{N2} and Γ_{N3}. Non-homogeneous Dirichlet boundary conditions are applied at the left and right boundaries of the domain, Γ_{D1} and Γ_{D2}. The magnitudes for these values are chosen based on the anticipated flow field that will result from the hydraulic head differences at the upstream and downstream faces of the dam. Pressure head values that vary linearly with height z are assumed and the boundary conditions can be summarized as:

$$\begin{cases} p^w = z + 100 & \text{on} \quad \Gamma_{D1} \\ p^w = 30 - z & \text{on} \quad \Gamma_{D2} \\ \frac{\partial p^w}{\partial n} = 0 & \text{on} \quad \Gamma_{N1} \cup \Gamma_{N2} \cup \Gamma_{N3} \end{cases} \tag{52}$$

The equipotential lines obtained from simulations with refinements using coarse and fine meshes are shown in Figures 16b and 16c, respectively. The pressure heads vary between 120 kPa, at the left boundary, and 10 kPa, at the right boundary. These correspond to hydraulic heads of approximately 12m and 1m at the upstream and downstream faces of the dam, respectively.

5.4.2. Results. We start the adaptive simulation for the cutoff problem with a relatively coarse mesh of around 300 degrees of freedom. The polynomial degrees are varied between $p = 2$, $p = 3$ and $p = 4$. The problem is also simulated using standard linear finite elements, $p = 1$, for comparison with FEA. The refinement parameter β in this case is selected as 10% and a structured mesh adaptive refinement strategy is used.

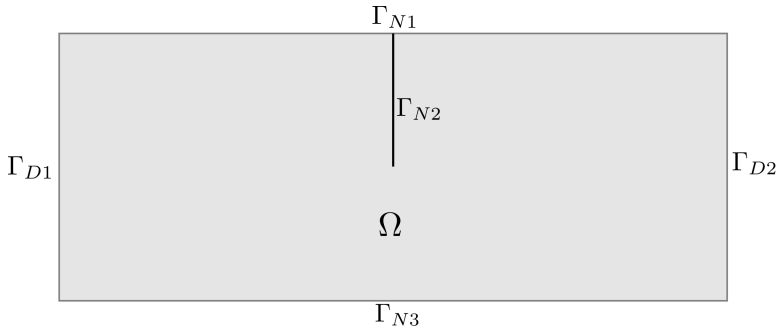

(a) Domain

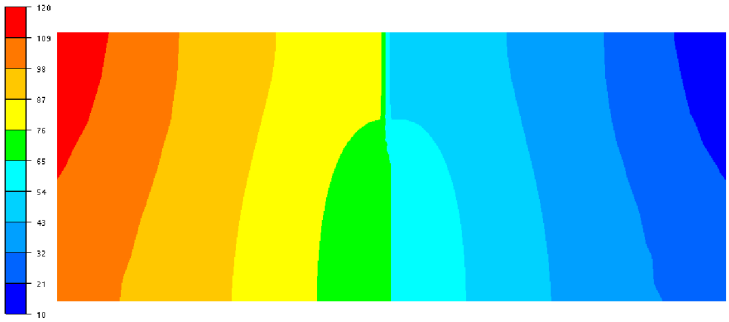

(b) Equipotential lines, $ndof = 315$

(c) Equipotential lines, $ndof = 5715$

Figure 16. **The cutoff wall problem**: Domain with boundary conditions and equipotential lines for coarse and fine meshes. The maximum and minimum pressure head values are 120 kPa and 10 kPa.

The pressure profiles obtained using a coarse mesh could show significant discretization errors. This is illustrated by plotting horizontal and vertical pressure profile plots for coarse and locally refined meshes around the cutoff wall. Figure 17a shows horizontal pressure profiles 2m above the tip of the cutoff wall, plotted over a horizontal distance of 25m, 12.5m on both sides of the cutoff wall. Notice the significant difference in pressure drop over the cutoff wall, i.e. 71.1-58.9 = 12.2 kPa and 75.5-54.5 = 21.0 kPa for the coarse mesh and fine mesh, respectively. This corresponds to more than 40% underestimation of the pressure drop calculated by the coarse mesh, which affects the expected effect of water flow at the downstream base of the dam. Vertical pressure profiles at the location of the cutoff wall, and spanning over the entire height of the domain, are shown in Figure 17b. Again, we observe significant differences in the obtained solutions.

The physical meshes obtained at selected refinement steps are shown in Figure 18. The meshes and the resulting number of degrees of freedom for $p = 2$ at the 4th and 12th refinement steps are shown in Figures 18a and 18b. The corresponding results for $p = 3$ are shown in Figures 18c and 18d, whereas Figures 18e and 18f show those for $p = 4$. At large refinement numbers, extra

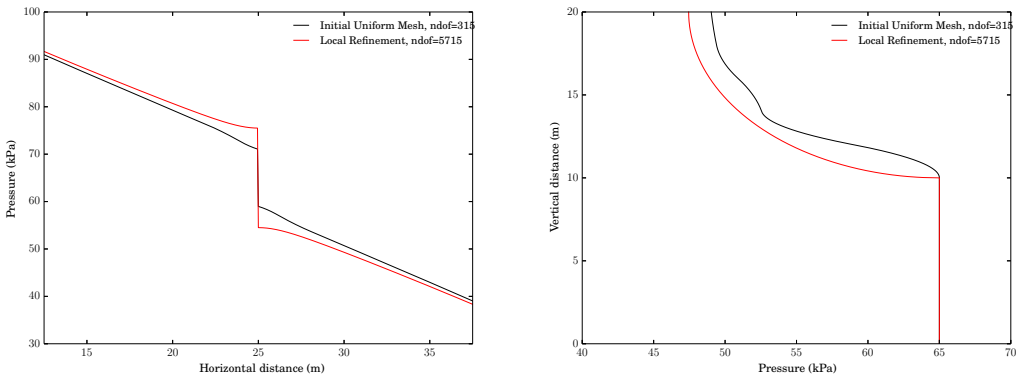

(a) (b)

Figure 17. **The cutoff wall problem**: Horizontal and vertical pressure profile plots

refinements are observed at the boundaries where non-homogeneous Dirichlet boundary conditions are applied since these are only approximated.

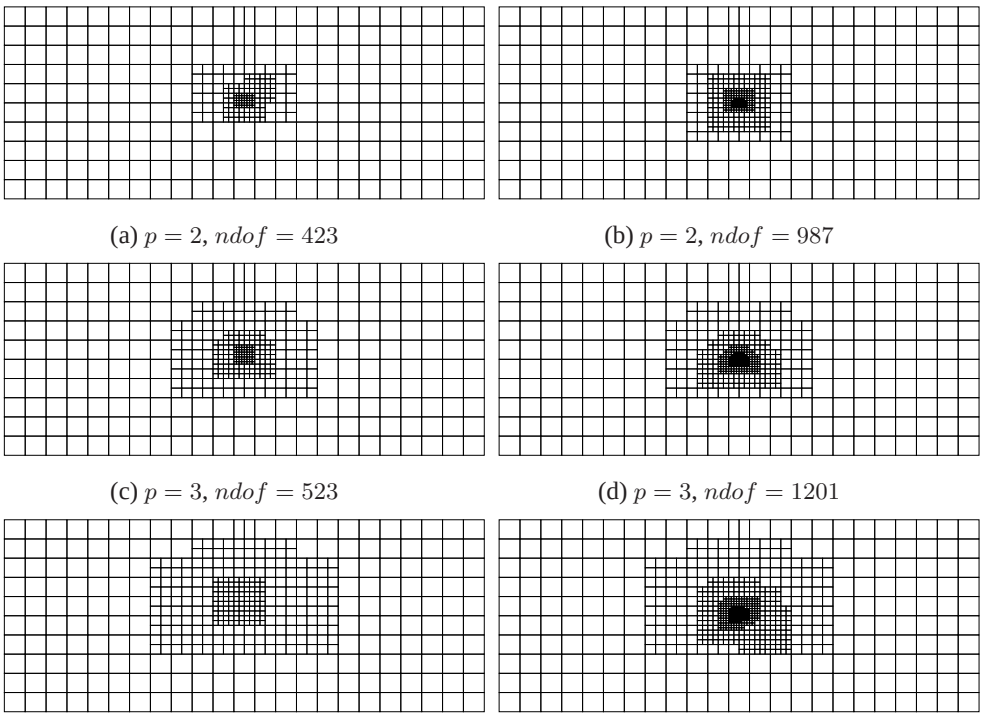

(a) $p = 2$, $ndof = 423$ (b) $p = 2$, $ndof = 987$

(c) $p = 3$, $ndof = 523$ (d) $p = 3$, $ndof = 1201$

(e) $p = 4$, $ndof = 560$ (f) $p = 4$, $ndof = 1369$

Figure 18. **The cutoff wall problem**: Adaptive meshes at different refinement steps for the selected $\beta = 10\%$. Each column represents the same refinement step for varying polynomial degrees.

The convergence plots comparing the relative errors from uniform and local refinement are shown in Figure 19. The results from a FEA using standard linear finite elements, $p = 1$, are included for comparison. For linear elements, FEA and IGA result in similar basis functions and we use this fact to compare the FEA results with local refinement using linear LR B-splines. We observe that local refinement performs slightly better in this case. The uniform refinement simulations with higher order polynomials show that the results are only marginally better in recovering errors compared

to the FEA results. Local refinement simulation using higher order polynomials, however, show good convergence properties. Optimal convergence rates are obtained for $p = 2$ and $p = 3$ for the maximum number of degrees of freedom specified in the adaptive simulation. The convergence rate appears to improve for $p = 4$ but requires more refinement steps to reach an optimal order, thereby increasing the total number of degrees of freedom.

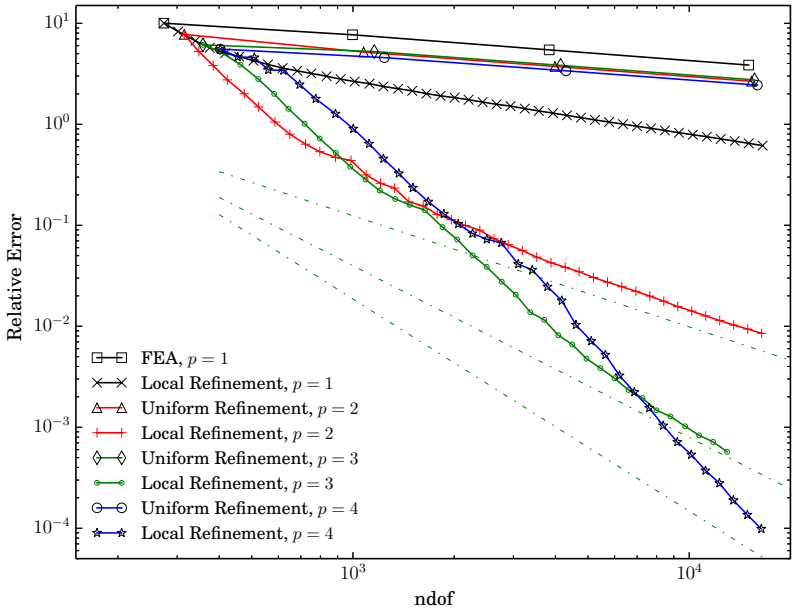

Figure 19. **The cutoff wall problem**: Convergence plots

5.5. Flow in a heterogeneous medium

The errors observed in the numerical simulation of groundwater flow in heterogeneous formations using coarse meshes could be very significant, [19]. Using a very fine mesh for such cases helps in reducing these errors but a uniform refinement throughout the domain implies unnecessarily fine meshes at locations where the errors are smaller. In such cases, adaptive simulation with local refinement could be more effective.

5.5.1. Problem definition. We consider a square domain of size $1m \times 1m$. The heterogeneous hydraulic conductivity k on the flow domain is assumed to follow a lognormal distribution. The probability density function for the lognormal distribution of k is:

$$f(k) = \frac{1}{\sigma k\sqrt{2\pi}} e^{-\frac{(\ln(k)-\mu)^2}{2\sigma^2}} \tag{53}$$

where μ is the mean and σ is the standard deviation of the normally distributed logarithm of the hydraulic conductivity. A random field with $\mu = -15$ and $\sigma = 7$ was generated.

For smoothing out the randomly generated data, a Gaussian filter of the form

$$g(x, y) = e^{-\frac{1}{3}\left(\frac{x^2}{l_x}+\frac{y^2}{l_y}\right)} \tag{54}$$

is applied. The filter dimensions in the x and y directions are chosen to be the same with values of $l_x = l_y = 20$. The smoothed data was truncated such that the hydraulic conductivity values vary between $10^{-3}m/s$ and $10^{-7}m/s$. The realization of the stationary random field generated is shown in Figure 20 in terms of color field and 3D plots.

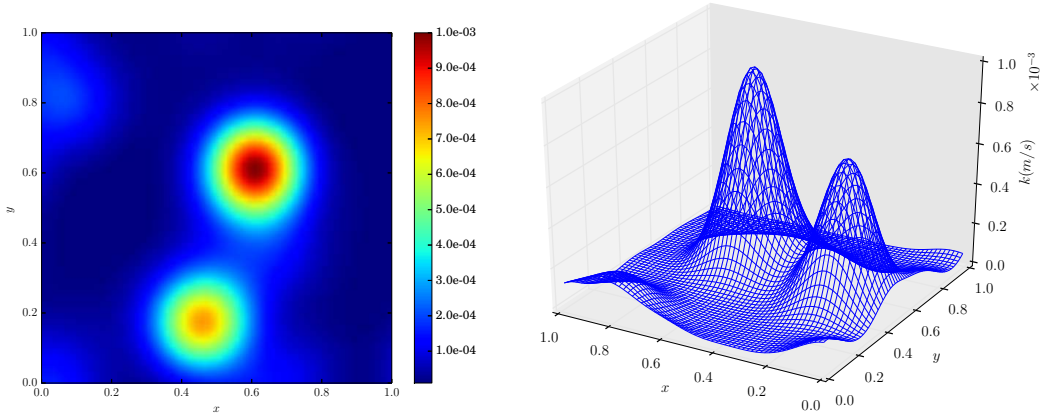

(a) Field plot (b) 3D plot

Figure 20. **The heterogeneous problem**: Realization of the randomly generated hydraulic conductivity field.

Dirichlet boundary conditions are applied on the left and right boundaries of the heterogeneous square domain to create a pressure gradient. The top and bottom boundaries of the domain are represented by homogeneous Neumann (no-flux) boundary conditions. An illustration of the applied boundary conditions is shown in Figure 21a. These boundary conditions are:

$$\begin{cases} p^w = 1000 & \text{on} \quad \Gamma_{D1} \\ p^w = 0 & \text{on} \quad \Gamma_{D2} \\ \frac{\partial p^w}{\partial n} = 0 & \text{on} \quad \Gamma_{N1} \cup \Gamma_{N2} \end{cases} \tag{55}$$

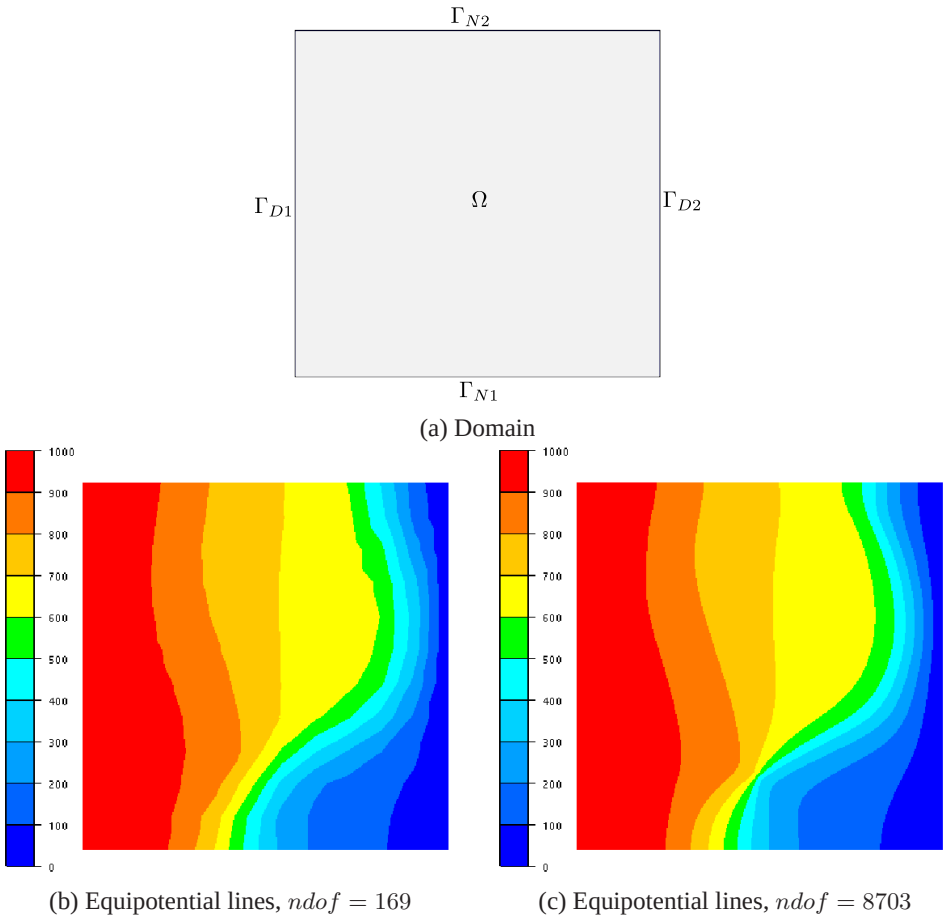

(a) Domain

(b) Equipotential lines, $ndof = 169$

(c) Equipotential lines, $ndof = 8703$

Figure 21. **The heterogeneous problem**: Simulation domain with boundary conditions and equipotential lines for coarse and fine meshes.

The equipotential lines obtained from simulation with uniform refinement using coarse and fine meshes are shown in Figures 21b and 21c, respectively. The difference in the hydraulic conductivity within the domain creates preferential flow paths and this results in very large changes in the pressure gradient at some locations of the domain.

5.5.2. Results. The heterogeneous problem is simulated starting from a relatively coarse mesh with number of degrees of freedom being around 170. Polynomial degrees of $p = 2$ and $p = 3$ are considered and the refinement parameter β in this case is selected as 10%. The resulting physical meshes for selected refinement steps are shown in Figure 22. In particular, Figures 22a-22c show the locally refined meshes for $p = 2$, whereas Figures 22d-22f show those for $p = 3$.

The convergence plots comparing local and uniform refinements for $p = 2$ and $p = 3$ are shown in Figure 23. The plots indicate that the convergence rate gained by using local refinement is not very significant. The reason for this is that, unlike complex boundary conditions which could imply strong singularities, varying material behavior is a weak discontinuity. The error recovery using local refinement, however, could be more significant compared to uniform refinement for simulations over large heterogeneous domains.

The random hydraulic conductivity field considered in Figure 20 shows a very large variability in the conductivity values. In some cases, the hydraulic conductivity fields in heterogeneous aquifers could show variability of a lesser magnitude within the domain. One such lognormal random field is generated and shown in Figure 24. The random field is generated by assuming a mean $\mu = -10$ and a variance $\sigma^2 = 2$. The filter dimensions in this case are taken as $l_x = 1$ and $l_y = 15$. The hydraulic

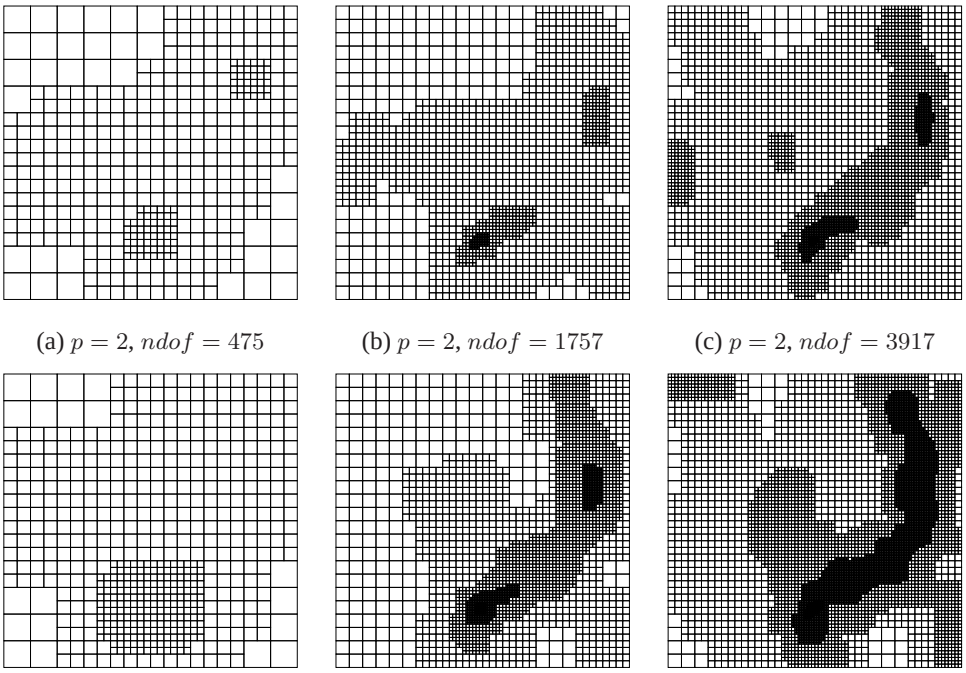

(a) $p = 2$, $ndof = 475$ (b) $p = 2$, $ndof = 1757$ (c) $p = 2$, $ndof = 3917$

(d) $p = 3$, $ndof = 631$ (e) $p = 3$, $ndof = 2977$ (f) $p = 3$, $ndof = 7429$

Figure 22. **The heterogeneous problem**: Adaptive meshes at different refinement steps for the selected $\beta = 10\%$. Each column represents the same refinement step for varying polynomial degrees.

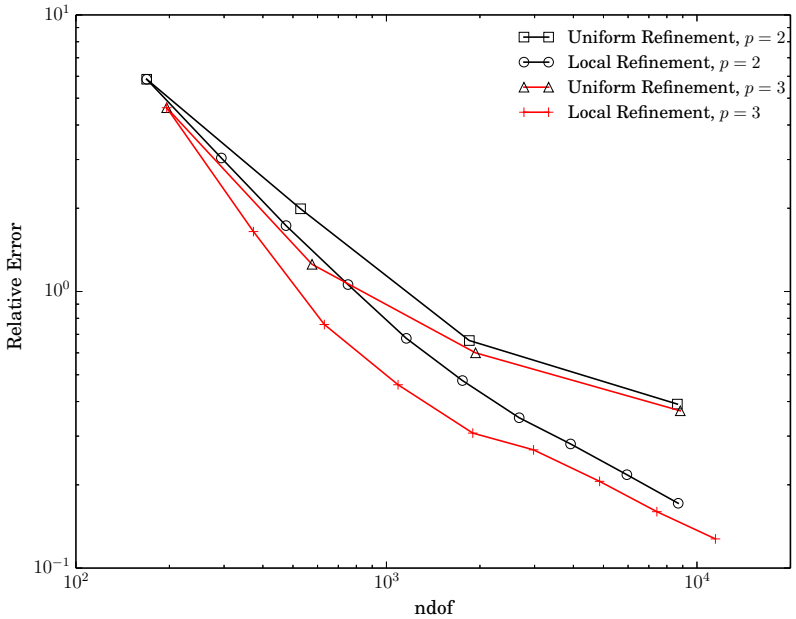

Figure 23. **The heterogeneous problem**: Convergence plots

conductivity values vary by an order of magnitude of 10. Adaptive simulations were performed with $p = 2$ and $p = 3$, using $\beta = 20\%$. The resulting adaptive meshes at selected refinement steps

are shown in 25. The difference in convergence rates between uniform and local refinement for this case is small and is not shown here.

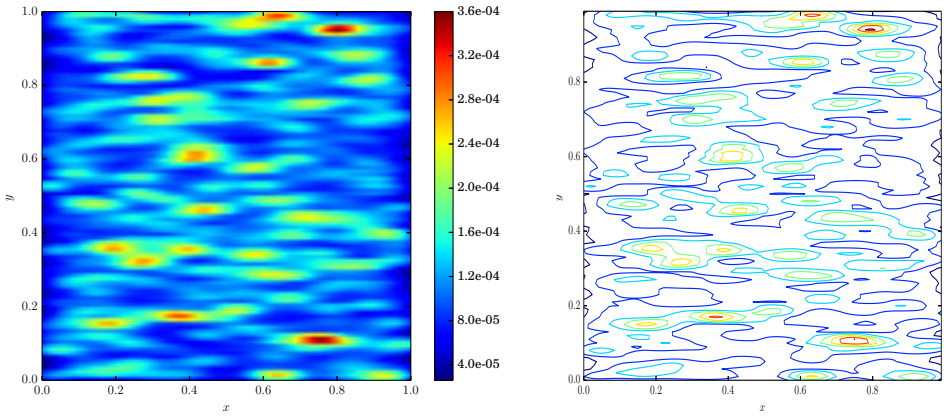

(a) Field plot (b) Contour plot

Figure 24. **The heterogeneous problem**: Realization of the randomly generated hydraulic conductivity field.

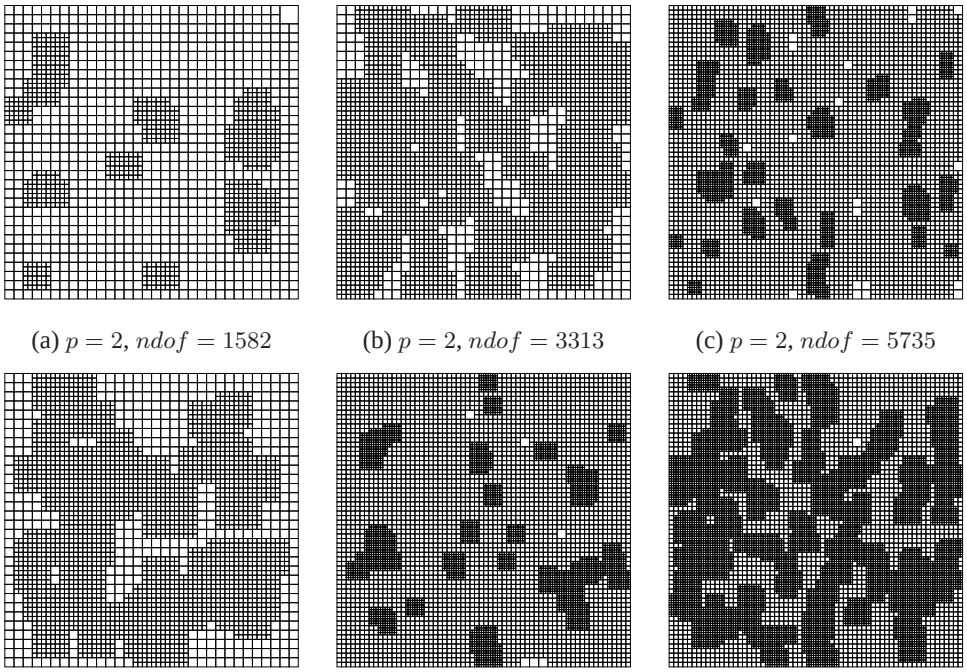

(a) $p = 2$, $ndof = 1582$ (b) $p = 2$, $ndof = 3313$ (c) $p = 2$, $ndof = 5735$

(d) $p = 3$, $ndof = 2791$ (e) $p = 3$, $ndof = 5860$ (f) $p = 3$, $ndof = 10156$

Figure 25. **The heterogeneous problem**: Adaptive meshes at different refinement steps for the selected $\beta = 20\%$. Each column represents the same refinement step for varying polynomial degrees.

Material property variation in other cases maybe of a non-homogeneous type and such a problem may be handled depending on the strength of the discontinuity introduced by the non-homogeneity. Weak discontinuities, such as material interfaces in a domain with layered materials, can be simulated accurately by ensuring C^0 continuity at the interfaces, without requiring adaptive refinement. This is achieved in IGA by making the multiplicity of the knots, m, at the interfaces equal to the polynomial degree, p, used i.e. C^{p-m} continuity. Strong discontinuities, such as cracks and impervious interfaces, result in jumps in the computed solution and introduce singularities depending on their location in the flow domain. These features can be simulated by introducing C^{-1} discontinuities, which is one of the powerful features of IGA. The cutoff wall example in Section 5.4 represents a special case of such strong discontinuities.

6. CONCLUDING REMARKS

Steady-state groundwater flow problems with varying numerical challenges were studied using adaptive isogeometric analysis with locally refined (LR) B-splines. In particular, the problems studied were flow around an impervious corner, flow around a cutoff wall, flow in a heterogeneous medium and flow in a discontinuous material field. The simulations were performed using both local and uniform refinement. The adaptive simulations with local refinement rely on a posteriori error estimates as a refinement criteria where the error estimates are based on Continuous Global L_2-projection (CGL2) of the computed solution. The effectivity of the error estimator was verified with benchmark problems which have analytical solutions, before being used in the application examples. In general, adaptive simulations with local refinement were observed to outperform simulations with uniform refinement in terms of error recovery. Optimal convergence rates were obtained for problems with strong singularities where the rates were observed to improve with increasing polynomial orders. Application to problems with weak discontinuities, due to material property variation, shows that optimal convergence rates may not be achieved but adaptive refinement still performed better than uniform refinement in error recovery. Local refinement could especially be more useful for large scale groundwater flow problems, with singularities and/or discontinuities, where simulations with uniform refinement could be computationally expensive.

In the present study, only two-dimensional groundwater flow problems were studied. Application to three-dimensional problems, however, is straight forward where the mathematical procedures are a simple extension of the formulations presented in Section 3.1.2. In particular, we will have trivariate functions for three-dimensional problems based on three knot vectors in each direction. As in the bivariate case, the refinements are performed in one parametric domain at a time as illustrated in Eq. 17.

A. SOURCE FUNCTION AND SECONDARY SOLUTION FOR THE WAVEFRONT PROBLEM

The source function f corresponding to the assumed analytical solution of the wavefront problem numerical example in Section 5.2.1 is given by:

$$f = \left[\frac{250000(a-0.25)}{a^2b^2} + \frac{50}{a^3b}\right]\left[c(x-0.5)^2 + (y-0.5)^2\right] - \frac{50(c+1)}{ab}$$

where:

$$a = \sqrt{(x-0.5)^2 + (y-0.5)^2}$$
$$b = 2500\left[a-0.25\right]^2 + 1$$
$$c = \frac{\kappa_x}{\kappa_y} \quad \Rightarrow \text{Degree of anisotropy}$$

The secondary solution, i.e. the velocity, for the wavefront problem is derived from the Darcy equation as:

$$\mathbf{v} = -\frac{50}{ab}\begin{Bmatrix} c(x-0.5) \\ (y-0.5) \end{Bmatrix}$$

ACKNOWLEDGEMENTS

This work is financially supported by the Research Council of Norway and industrial partners through the research project SAMCoT, Sustainable Arctic Marine and Coastal Technology. The authors gratefully acknowledge the support. Special thanks to all in the IFEM software team at SINTEF Applied Mathematics and Dr. Kjetil A. Johannessen for his work on LR B-splines.

REFERENCES

1. Finn WDL. Finite-element analysis of seepage through dams. *Journal of Soil Mechanics & Foundations Div*, ASCE SM6, 92:41-48, 1967.
2. Pinder GF, Frind EO. Application of Galerkin's procedure to aquifer analysis. *Water Resources Research*, 8(1):108–120, 1972.
3. Reeves M, Duguid JO. Water movement through saturated-unsaturated porous media: A finite-element Galerkin model. Technical report, Oak Ridge National Lab., Tenn.(USA), 1975.
4. Gupta SK, Cole CR, Pinder GF. A finite-element three-dimensional groundwater (FE3DGW) model for a multiaquifer system. *Water resources research*, 20(5):553–563, 1984.
5. Yeh GT. On the computation of darcian velocity and mass balance in the finite-element modeling of groundwater-flow. *Water Resources Research*, 17(5):1529–1534, 1981.
6. Botha JF, Bakkes GN. Galerkin finite element method and the groundwater flow equation: 1. convergence of the method. *Advances in Water Resources*, 5(2):121–126, 1982.
7. Tharp TM. An enriched finite-element for simulation of groundwater-flow to a well or drain. *Journal of Hydrology*, 55(1-4):237–245, 1982.
8. Dogrul EC, Kadir TN. Flow computation and mass balance in Galerkin finite-element groundwater models. *Journal of Hydraulic Engineering-Asce*, 132(11):1206–1214, 2006.
9. Lafe OE, Liu PLF, Liggett JA, Cheng AHD, Montes JS. Singularities in Darcy flow through porous media. *Journal of the Hydraulics Division*, 106(6):977–997, 1980.
10. Liang D, Zhang B. A finite element method for a unidimensional single-phase nonlinear free boundary problem in groundwater flow. *IMA Journal of Numerical Analysis*, 19(4):563–581, 1999.
11. Neuman SP, Witherspoon PA. Finite element method of analyzing steady seepage with a free surface. *Water Resources Research*, 6(3), 1970.
12. Larabi A, De Smedt F. Numerical solution of 3-D groundwater flow involving free boundaries by a fixed finite element method. *Journal of Hydrology*, 201(1-4):161–182, 1997.
13. Rank E, Werner H. An adaptive finite-element approach for the free-surface seepage problem. *International Journal for Numerical Methods in Engineering*, 23(7):1217–1228, 1986.
14. Sharif NH, Wiberg NE. Adaptive ICT procedure for non-linear seepage flows with free surface in porous media. *Communications in Numerical Methods in Engineering*, 18(3):161–176, 2002.
15. Boeriu S, Bruch JC. Performance analysis tools applied to a finite element adaptive mesh free boundary seepage parallel algorithm. *Computer Methods in Applied Mechanics and Engineering*, 194(2-5):297–312, 2005.
16. Jie YX, Liu LZ, Xu WJ, Li GX. Application of nem in seepage analysis with a free surface. *Mathematics and Computers in Simulation*, 89:23–37, 2013.
17. Burkley VJ, Bruch JC. Adaptive error analysis in seepage problems. *International Journal for Numerical Methods in Engineering*, 31(7):1333–1356, 1991.
18. Smaoui H, Zouhri L, Ouahsine A, Carlier E. Modelling of groundwater flow in heterogeneous porous media by finite element method. *Hydrological Processes*, 26(4):558–569, 2012.
19. Cao J, Kitanidis PK. Adaptive-grid simulation of groundwater flow in heterogeneous aquifers. *Advances in Water Resources*, 22(7):681–696, 1999.
20. George K, Thomas H. Simulation of groundwater flow based on adaptive mesh refinement. *Proceedings of the 7th International Congress on Environmental Modeling and Software, Eds Daniel P. Ames, Nigel W.T. Quinn and Andrea E. Rizzoli*, 2014.
21. Dokken T, Lyche T, Pettersen KF. Polynomial splines over locally refined box-partitions. *Computer Aided Geometric Design*, 30(3):331–356, 2013.
22. Johannessen KA, Kvamsdal T, Dokken T. Isogeometric analysis using LR B-splines. *Computer Methods in Applied Mechanics and Engineering*, 269(0):471–514, 2014.
23. Hughes TJR, Cottrell JA, Bazilevs Y. Isogeometric analysis: CAD, finite elements, NURBS, exact geometry and mesh refinement. *Computer Methods in Applied Mechanics and Engineering*, 194(39-41):4135–4195, 2005.
24. Sederberg TW, Zheng J, Bakenov A, Nasri A. T-splines and T-NURCCs. *ACM Trans. Graph.*, 22(3):477–484, 2003.
25. Cottrell JA, Hughes TJR, Bazilevs Y. *Isogeometric Analysis: Toward Integration of CAD and FEA*. Wiley, Chichester, West Sussex, U.K., Hoboken, NJ, 2009.

26. Babuška I, Rheinboldt WC. Error estimates for adaptive finite element computations. *SIAM Journal on Numerical Analysis*, 15(4):736–754, 1978.
27. Babuška I, Rheinboldt WC. A posteriori error estimates for the finite element method. *International Journal of Numerical Methods and Engineering*, 12:1597–1615, 1978.
28. Ainsworth M, Oden JT. *A posteriori error estimation in finite element analysis*. Pure and Applied Mathematics (New York). Wiley-Interscience [John Wiley & Sons], New York, 2000.
29. Zienkiewicz OC, Zhu JZ. A simple error estimator and adaptive procedure for practical engineering analysis. *Internat. J. Numer. Methods Engrg.*, 24(2):337–357, 1987.
30. Zienkiewicz OC, Zhu JZ. The superconvergent patch recovery and a posteriori error estimates. I. The recovery technique. *International Journal for Numerical Methods in Engineering*, 33(7):1331–1364, 1992.
31. Zienkiewicz OC, Zhu JZ. The superconvergent patch recovery and a posteriori error estimates. II. Error estimates and adaptivity. *International Journal for Numerical Methods in Engineering*, 33(7):1365–1382, 1992.
32. Kvamsdal T, Okstad KM. Error estimation based on superconvergent patch recovery using statically admissible stress fields. *International Journal for Numerical Methods in Engineering*, 42(3):443–472, 1998.
33. Okstad KM, Kvamsdal T, Mathisen KM. Superconvergent patch recovery for plate problems using statically admissible stress resultant fields. *International journal for numerical methods in engineering*, 44(5):697–727, 1999.
34. Kvamsdal T, Okstad KM, Herfjord K. Error estimator for recovered surface forces in incompressible Navier-Stokes flow. *Proceedings for The 17th International Conference on Offshore Mechanics and Arctic Engineering, Lisbon, Portugal*, 1998.
35. Kvamsdal T. Variationally consistent postprocessing for adaptive recovery of stresses. *Proceedings for European Conference on Computational Mechanics*, 1999.
36. Melbø H, Kvamsdal T. Goal oriented error estimators for Stokes equations based on variationally consistent postprocessing. *Computer Methods in Applied Mechanics and Engineering*, 192(5–6):613–633, 2003.
37. Okstad KM, Kvamsdal T. Object-oriented programming in field recovery and error estimation. *Engineering with Computers*, 15(1):90–104, 1999.
38. Okstad KM, Kvamsdal T. Object-oriented field recovery and error estimation in finite element methods. In H. P. Langtangen, A. M. Bruaset, and E. Quak, editors, *Advances in Software Tools for Scientific Computing*, volume 10 of *Lecture Notes in Computational Science and Engineering*, pages 283–317. Springer Berlin Heidelberg, 2000.
39. Kumar M, Kvamsdal T, Johannessen KA. Simple posteriori error estimators in adaptive isogeometric analysis. *Computers and Mathematics with Applications*, doi:10.1016/j.camwa.2015.05.031.
40. Kumar M, Kvamsdal T, Johannessen KA. Superconvergent patch recovery and a posteriori error estimation technique in adaptive isogeometric analysis. *Computer Methods in Applied Mechanics and Engineering*, Submitted, 2015.
41. Wahlbin LB. *Superconvergence in Galerkin finite element methods.* Lecture Notes in Mathematics, Volume 1605. Springer-Verlag, Berlin, 1995
42. Mitchell WF. A collection of 2D elliptic problems for testing adaptive algorithms. Technical Report NISTIR 7668, U.S. Department of Commerce, Technology Administration, National Institute of Standards and Technology, Gaithersburg, MD, USA, 2010.